

STRONG FIELD-TO-FIELD VARIATION OF Ly α NEBULAE POPULATIONS AT $z \simeq 2.3$

YUJIN YANG^{1,2}, ANN ZABLUDOFF², DANIEL EISENSTEIN², ROMEEL DAVÉ²
ApJ in press

ABSTRACT

Understanding the nature of distant Ly α nebulae, *aka* “blobs,” and connecting them to their present-day descendants requires constraining their number density, clustering, and large-scale environment. To measure these basic quantities, we conduct a deep narrowband imaging survey in four different fields, Chandra Deep Field South (CDFs), Chandra Deep Field North (CDFN), and two COSMOS subfields, for a total survey area of 1.2 deg². We discover 25 blobs at $z = 2.3$ with Ly α luminosities of $L_{\text{Ly}\alpha} = 0.7\text{--}8 \times 10^{43}$ ergs s⁻¹ and isophotal areas of $A_{\text{iso}} = 10\text{--}60 \square''$. The transition from compact Ly α emitters ($A_{\text{iso}} \sim \text{a few } \square''$) to extended Ly α blobs ($A_{\text{iso}} > 10 \square''$) is continuous, suggesting a single family perhaps governed by similar emission mechanisms. Surprisingly, most blobs (16/25) are in one survey field, the CDFS. The six brightest, largest blobs with $L_{\text{Ly}\alpha} \gtrsim 1.5 \times 10^{43}$ ergs s⁻¹ and $A_{\text{iso}} > 16 \square''$ lie *only* in the CDFS. These large, bright blobs have a field-to-field variance of $\sigma_v \gtrsim 1.5$ (150%) about their number density $n \sim 1.0_{-0.6}^{+1.8} \times 10^{-5}$ Mpc⁻³. This variance is large, significantly higher than that of unresolved Ly α emitters ($\sigma_v \sim 0.3$ or 30%), and can adversely affect comparisons of blob number densities and luminosity functions among different surveys. Our deep, blind survey allows us to construct a reliable blob luminosity function. We compare the statistics of our blobs with dark matter halos in a 1 h^{-1} Gpc cosmological N-body simulation. At $z = 2.3$, n implies that each bright, large blob could occupy a halo of $M_{\text{halo}} \gtrsim 10^{13} M_{\odot}$ if most halos have detectable blobs. The predicted variance in n is consistent with that observed and corresponds to a bias of ~ 7 . Blob halos lie at the high end of the halo mass distribution at $z = 2.3$ and are likely to evolve into the $\sim 10^{14} M_{\odot}$ halos typical of galaxy clusters today. On larger scales of ~ 10 co-moving Mpc, blobs cluster where compact Ly α emitters do, indicating that blobs lie in coherent, highly overdense structures.

Subject headings: galaxies: formation — galaxies: high-redshift — intergalactic medium

1. INTRODUCTION

Ly α nebulae, or “blobs,” are extended sources at $z \sim 2\text{--}6$ with typical Ly α sizes of $\gtrsim 5''$ ($\gtrsim 50$ kpc) and line luminosities of $L_{\text{Ly}\alpha} \gtrsim 10^{43}$ ergs s⁻¹ (e.g., Keel et al. 1999; Steidel et al. 2000; Francis et al. 2001; Matsuda et al. 2004; Dey et al. 2005; Smith & Jarvis 2007; Hennawi et al. 2009; Prescott et al. 2009; Yang et al. 2009). Because the large spatial extent of their Ly α -emitting gas implies an interaction between the surrounding intergalactic medium and any embedded galaxies, blobs may signal an important phase of galaxy formation in the early universe, including cold gas accretion (Haiman, Spaans, & Quataert 2000; Fardal et al. 2001; Yang et al. 2006; Dijkstra & Loeb 2009), galactic-scale feedback due to stellar winds (Taniguchi & Shioya 2000), or intense radiative feedback from AGN (Geach et al. 2009). Despite the importance of blobs and the controversy regarding their origins, even basic properties such as their number density, clustering, and large-scale environment are poorly constrained.

To understand into what these mysterious objects will evolve in the present day universe, measuring their statistics is critical due to the direct connection of number density and field-to-field variance to halo mass in Λ CDM cosmology. Currently, the halo mass of blobs is unknown.

Using the spatial extent and line-width of the Ly α line, Matsuda et al. (2006) estimate dynamical masses of $0.5\text{--}20 \times 10^{12} M_{\odot}$ if the extended Ly α emission is from gravitationally bound gas clouds and the resonant scattering of Ly α can be ignored.

The clustering of blobs has not been measured directly in past work, yet there are hints that it is strong. After surveying over ~ 4.8 deg² in the NOAO Deep-Wide Boötes field (Jannuzi & Dey 1999), Yang et al. (2009) discover just four bright blobs, yet two of them lie within only $\sim 70''$ of each other (see also the discovery of a Ly α blob near a radio-loud Ly α halo by Matsuda et al. 2009). Some, but not all (e.g., Gronwall et al. 2007; Nilsson et al. 2009), narrowband surveys targeting *compact* Ly α emitters also detect blobs at similar redshifts. For example, while following up the two bright blobs found by Steidel et al. (2000) in the SSA22 field, Matsuda et al. (2004) discover a spectacular clustering of 35 blobs, in which the two brightest lie at the intersection of filaments traced by compact Ly α emitters (Matsuda et al. 2005). Palunas et al. (2004) discover two³ additional Ly α blobs in the J2143-4423 region defined by an overdensity of compact Ly α emitters (Francis et al. 2001). To measure directly the number density and clustering of Ly α blobs, and thus to constrain their halo mass, requires a large volume survey, particularly over different sight lines, to account for any field-to-field variations. Furthermore, one must apply

¹ Max-Planck-Institut für Astronomie, Königstuhl 17, D-69117, Heidelberg, Germany. yyang@mpia.de

² Steward Observatory, University of Arizona, 933 North Cherry Avenue, Tucson AZ 85721

⁴ One of these blob candidates has now been identified as a low- z interloper (J. Colbert priv. comm.)

uniform selection criteria for identifying blobs over the entire survey volume.

To acquire a large, unbiased sample of Ly α blobs at $z = 2.3$, we have pursued two complimentary narrow-band imaging surveys. The shallow, but wide sky coverage, survey using the Steward Observatory Bok 2.3m + 90Prime imager targets rare, luminous Ly α blobs ($L_{\text{Ly}\alpha} \gtrsim 2 \times 10^{43}$ ergs s $^{-1}$; Yang et al. 2009). In this paper, we report the first results from our deeper, but smaller sky coverage, survey with the NOAO 4m telescopes and MOSAIC imagers that targets presumably more common intermediate size and luminosity Ly α blobs like those discovered by Matsuda et al. (2004). Using blob statistics from the four different 30' \times 30' survey fields, in the Chandra Deep Field-South (CDFN; Brandt et al. 2001), Chandra Deep Field-North (CDFN; Giacconi et al. 2002), and two regions of the Cosmic Evolution Survey (COSMOS; Scoville et al. 2007; Koekemoer et al. 2007), we determine the field-to-field variation in the blob number density. We then use a large volume cosmological N-body simulation to constrain their host halo masses for the first time.

In §2, we describe our narrow-band imaging survey and the data reduction procedures. §3 describes the selection of the Ly α blob sample. In §4, we present the Ly α blob candidates (§4.1), compare their sizes and luminosities to those of compact Ly α sources (§4.2), constrain their field-to-field variation and halo masses (§4.3), and characterize their large-scale environment using the compact Ly α emitters (§4.4). In §5, we discuss our conclusions. Throughout this paper, we adopt the cosmological parameters $H_0 = 100 h$ km s $^{-1}$ Mpc $^{-1}$, $h = 0.7$, $\Omega_M = 0.3$, and $\Omega_\Lambda = 0.7$. All magnitudes are in the AB system (Oke 1974).

2. OBSERVATIONS AND DATA REDUCTION

Using the MOSAIC-I and II CCD imagers on the KPNO Mayall and the CTIO Blanco 4m telescopes, we obtain deep narrowband images with a custom narrowband filter (hereafter NB403 or NB). This narrowband filter has a central wavelength of $\lambda_c \approx 4030\text{\AA}$, designed for selecting Ly α -emitting sources at $z \approx 2.3$. Its bandwidth of $\Delta\lambda_{\text{FWHM}} \approx 45\text{\AA}$ provides a line-of-sight depth of $\Delta z \approx 0.037$, corresponding to 46.8 Mpc at $z = 2.3$ in the comoving frame. The CDFS, CDFN, and COSMOS survey fields have extensive ancillary data sets, including the deepest X-ray images for robust identification of AGN.

We conducted the narrowband imaging observations over nine photometric nights between January 2007 and February 2009. The MOSAIC I and II cameras have eight $2k \times 4k$ CCDs with a pixel scale of $0''.27$ pixel $^{-1}$, leading to a sky coverage of $37' \times 37'$. We obtain deep narrowband images for four different pointings: CDFS, CDFN, and two COSMOS subfields (hereafter COSMOS1 and COSMOS2). The total exposure time ranges from 7.2 to 10 hr, which consists of individual 20 or 30 minute exposures with a standard dither pattern to fill in the gaps between the eight chips. The seeing ranges from $1''.0$ to $1''.3$ depending on the fields. Table 1 summarizes our narrowband observations, including the central coordinates of the survey fields, total exposure times, survey areas, seeing, and survey depths.

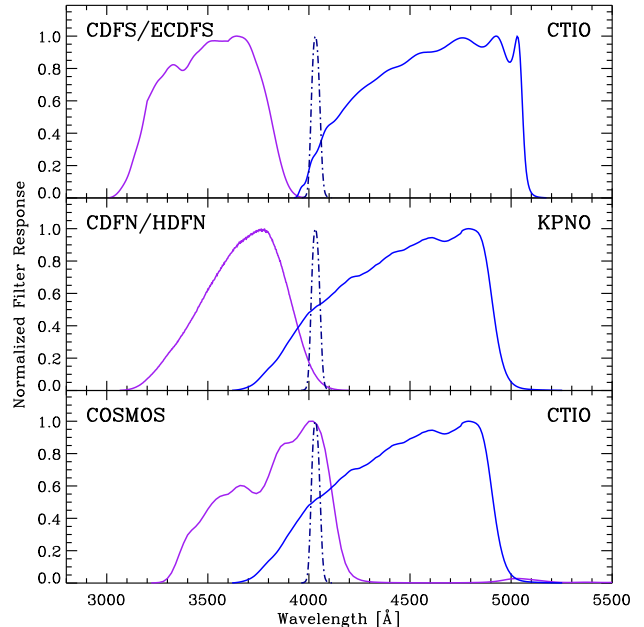


FIG. 1.— Filter response profiles for the NB403 narrowband (*dotted line*) and broadband (*U* and *B*) filters (*solid lines*) used in this study. The profiles are normalized to a maximum throughput of 1 and include the transmission of the atmosphere, telescope, camera optics, filter, and detector. (*Top*) ESO 2.2m *U* and *B* band filters from MUSYC (Gawiser et al. 2006a,b). (*Middle*) KPNO *U* and Subaru *B* filters from the Hawaii-HDF survey (Capak et al. 2004). (*Bottom*) CFHT *u** and Subaru *B* filters from COSMOS (Capak et al. 2007).

To identify line emission objects requires that we subtract the continuum emission underlying the NB403 bandpass. We estimate the continuum using existing, deep broadband (*U* and *B*) images. For the CDFS, we use optical images from the Extended Chandra Deep Field-South dataset from the Multiwavelength Survey by Yale-Chile (MUSYC; Gawiser et al. 2006a,b)⁵. For the CDFN, we use the imaging products from the Hawaii Hubble Deep Field North survey (Capak et al. 2004). For COSMOS1 and COSMOS2, we use 25 image tiles for each subfield⁷ produced by Capak et al. (2007). For CDFS and CDFN, the broadband images have smaller sky coverage than our narrowband images, limiting our final survey areas (Table 1). Table 2 lists details of the broadband images, including the filter properties, survey depth, seeing, and the instruments used. We also show the narrow and broadband filter transmission curves for all fields in Figure 1.

We reduce the narrowband images with the IRAF *mscred* mosaic data reduction package (Valdes 1998) following the procedures of the NOAO Deep Wide Field Survey team (Jannuzi & Dey 1999). The data are corrected for crosstalk between amplifiers and bias-subtracted. For flat-fielding, we use dome flats together with night-sky

⁵ The original data were taken with the ESO MPG 2.2m and Wide Field Imager (WFI) by the ESO Deep Public Survey and COMBO-17 teams (Arnouts et al. 2001; Wolf et al. 2004; Erben et al. 2005; Hildebrandt et al. 2006). In this paper, we use the data products delivered by the MUSYC team.

⁷ The tile numbers for the lower-left and upper-right corners of COSMOS1 and COSMOS2 are (17, 69) and (65, 117), respectively.

flats, which are median-combined from unregistered object frames each night. Satellite trails, CCD edges, bad pixels, and saturated pixels are masked. The astrometry is calibrated with the USNO-B1.0 catalog (Monet et al. 2003) using the IRAF *ccmap* task. The individual images are transformed to have the same pixel scales and world coordinate systems (WCS) as the reference broadband images. For the COSMOS broadband images with finer pixel scale ($0''.15 \text{ pixel}^{-1}$), we resample them with the coarse MOSAIC-II pixel scale ($0''.27 \text{ pixel}^{-1}$) to make the reference images. Finally, the projected images are scaled using common stars in each frame and stacked to remove cosmic rays. For flux calibration, we employ the 3–5 spectrophotometric standard stars observed each night to derive extinction coefficients and zero points for the NB403 magnitudes. Typical uncertainties in the derived zero-points are 0.02–0.04 mag. These uncertainties are added to the photometry errors in quadrature.

In addition to the standard reduction procedures described above, we pay special attention to the “crosstalk” that occurs between CCDs (or amplifiers) sharing the readout electronics. The net effect of crosstalk is that a very bright or saturated source on one chip (or amplifier) produces echos or ghost images on the paired chips with proportional intensities, typically 0.02–0.2%, up to several counts. One can determine these proportionalities, known as crosstalk coefficients, using the science image itself, and thus remove echo images. In most circumstances, this crosstalk correction works well and does not affect the detection and photometry of bright sources. Furthermore, dithered exposures often average out the ghost images in the individual frames when stacked to make the final products.

However, residual ghost images from imperfect correction can be easily confused with low surface brightness objects. In particular, for CTIO MOSAIC-II, the crosstalk images of a source at pixel (x, y) on one chip appears at the same pixel coordinates on the other chips (victim chips). Therefore, ghost images always appear at the same location relative to real sources in the dithered exposures, and they will be co-added in the final combined images, leading to false detections mimicking diffuse extended emission.

To weed out false detections, we repeat the entire reduction procedure doubling the crosstalk coefficients so that the ghost images are over-corrected and appear as negative counts. If a blob candidate is indeed an artifact arising from imperfect correction, it will show up as a negative image in the final combined image. Figure 2 shows an example in which one artifact image appears as a negative mirror image, whereas a real object is not affected by this crosstalk over-correction. Note that the artifact is as bright as the real blob candidate, demonstrating that special care is required to reject false detections for extremely low-surface brightness objects like Ly α blobs.

3. SELECTION OF Ly α BLOB CANDIDATES

To find Ly α blob candidates, we construct photometric catalogs in the NB403 narrowband and two broadbands (U and B) using SExtractor (Bertin & Arnouts 1996). First, we make “detection” images ($NB+U+B$) by adding the NB403 and broadband images after scaling them according to their signal-to-noise ratios (S/N).

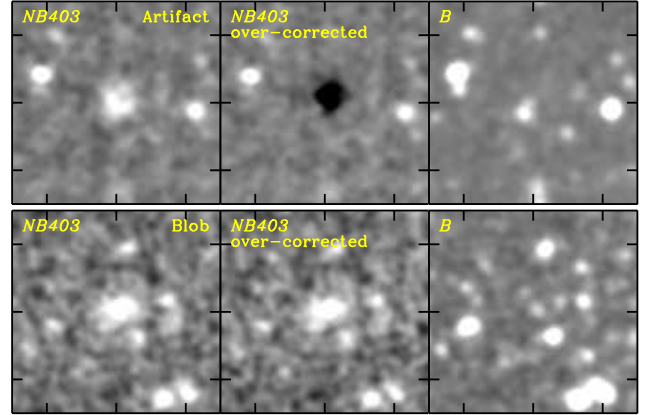


FIG. 2.— Distinguishing between a false detection arising from an imperfect crosstalk correction of the CTIO MOSAIC-II image and a true extended Ly α source. (From left to right) Original NB403 images, NB403 images over-corrected with crosstalk coefficients that are two times too large, and B band images. The ticks represent $10''$ intervals. Note that the residual due to the imperfect crosstalk correction arising from the standard reduction (*top left panel*) resembles an Ly α source that is spatially more extended than its continuum counterpart (*top right panel*). This artifact appears as a negative mirror image in the over-corrected image (*top middle panel*), while the real object is not affected by the crosstalk over-correction (*bottom middle panel*). By comparing the original and over-corrected images, we are able to reject false detections, which is critical given the small number statistics of the blob survey.

After identifying sources in the “detection” images that have least 2 pixels that are 1.5σ above the local sky, we run SExtractor in double-image mode on the NB403, U , and B images using these detection images. In other words, we first find the sources in the “detection” images and then obtain photometry at their position in the NB403, U , and B images to construct three separate (one narrow- and two broadband) catalogs. We adopt Kron-like elliptical aperture magnitudes (i.e., `MAG_AUTO` in SExtractor) to derive photometric properties. Our use of the “detection” images ensures that 1) all the sources detected in either NB or the broadbands are included in our catalog and 2) the elliptical apertures of the more extended sources in the ($NB+U+B$) image are large enough to include all the light from both the NB and broadband images. Note that this choice of photometric aperture is different from the classical Ly α emitter searches that adopt a small circular aperture (a few \times FWHM of seeing) to detect fainter sources.

The selection of Ly α blob candidates from the NB and broadband photometric catalogs consists of two steps: 1) selection for line (hopefully, Ly α) emitting objects with large line equivalent widths and 2) selection for spatially extended objects with a larger angular extent in line emission than in the broadbands. In other words, we define a “blob” as an object whose Ly α emission above a certain surface brightness threshold is more extended than its stellar continuum, thus representing light from the intergalactic medium.

First, we choose candidates by requiring that they are detected above the completeness limits of the NB403 images ($NB403 \lesssim 24.5 \text{ mag}$). All candidates must have observed-frame equivalent widths larger than 100\AA ($EW_{\text{rest}} > 30.3\text{\AA}$), corresponding to $(UB - NB) >$

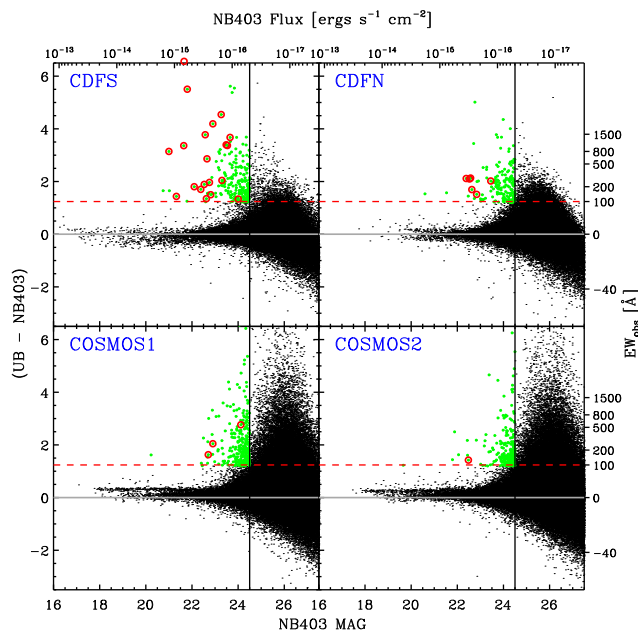


FIG. 3.— Color – magnitude ($UB-NB403$) versus $NB403$ diagram for all the sources detected in our four survey fields: CDFS, CDFN, and two COSMOS subfields. Here UB represents the AB magnitude of the average continuum flux density within the $NB403$ band estimated from the U and B band images. Right and top axes show the corresponding equivalent widths in the observed frame and the NB fluxes, respectively. We select line-emission objects with the criteria $NB < 24.5$ (solid line) and $(UB-NB403) > 1.2$ (dashed line; $EW_{\text{obs}} > 100\text{\AA}$). Open circles represent the final $\text{Ly}\alpha$ blob candidates obtained from Fig. 4. There are more open circles than final blob candidates in the CDFS panel because a few blob candidates include multiple sources.

1.2, where UB represents the AB magnitude of the average continuum flux density within the $NB403$ band (f_{cont}^{NB}) estimated from the U and B band images, $UB \equiv -2.5 \log(f_{\text{cont}}^{NB}) - 48.60$. We estimate f_{cont}^{NB} and the line flux (F_{line}) of these objects using the following relations:

$$f_{\text{cont}}^B = \frac{F_B - \epsilon_B F_{NB}}{\Delta\lambda_B - \Delta\lambda_{NB}} \quad (1)$$

$$f_{\text{cont}}^U = \frac{F_U - \epsilon_U F_{NB}}{\Delta\lambda_U - \Delta\lambda_{NB}}$$

$$f_{\text{cont}}^{NB} = \frac{1}{\lambda_B - \lambda_U} [(\lambda_B - \lambda_{NB})f_{\text{cont}}^B + (\lambda_{NB} - \lambda_U)f_{\text{cont}}^U]$$

$$F_{\text{line}} = F_{NB} - f_{\text{cont}}^{NB} \Delta\lambda_{NB},$$

where F_U , F_B and F_{NB} are the total flux in each filter derived from the U , B , and $NB403$ magnitudes, respectively. $\Delta\lambda_U$, $\Delta\lambda_B$, and $\Delta\lambda_{NB}$ represent the band-widths of the U , B and NB filters, respectively. f_{cont}^U and f_{cont}^B represent the average flux density of galaxy continuum within the U and B bands, respectively. ϵ_B and ϵ_U are the correction factors that we use to remove the NB light from each broadband when estimating f_{cont}^U and f_{cont}^B . Figure 3 shows the $(UB - NB)$ color as a function of NB magnitude for all objects detected in either the narrow or broad bands within our survey area.

In CDFS, COSMOS1, and COSMOS2, bright ($18 < NB < 22$) sources, mostly stars and nearby galaxies, have an average $(UB - NB)$ color that is consistent with zero (-0.11 ± 0.18 , 0.13 ± 0.17 , and 0.12 ± 0.12 , respectively).

In the CDFN, however, they have an average color of $(UB - NB) \sim -0.24 \pm 0.14$ mag, which suggests absorption features in our narrowband that are very unlikely. Because this -0.24 mag offset disappears when we adopt continuum measurements (in u and g) from the Sloan Digital Sky Survey, we apply a small correction (0.2 mag) to the CDFN broadband magnitudes (Capak et al. 2004) such that $(UB - NB) \simeq 0$ for the bright sources. Although we cannot explain the apparent problem with the CDFN broadband photometry in Capak et al. (2004), the selection of our blob sample is unaffected by the applied correction.

At our survey redshift, the only possible interlopers are nearby $[\text{O II}] \lambda 3727$ emitters at $z \approx 0.08$. However, such objects rarely have equivalent widths larger than 100\AA in the rest frame (Hogg et al. 1998). Therefore, we expect that the contamination of our $z = 2.3$ $\text{Ly}\alpha$ source catalog by nearby star forming galaxies is minimal.

Second, we identify those line-emission selected objects that are more spatially extended in $\text{Ly}\alpha$ than their continuum counterparts (Fig. 4). This selection definition is the same as that adopted by Matsuda et al. (2004) and somewhat different than that of Saito et al. (2006), who select spatially extended objects by requiring the FWHM in their intermediate-band to be larger than that in the broadband or continuum image (see also Nilsson et al. 2009).

We measure the spatial extent of the $\text{Ly}\alpha$ emission in the continuum-subtracted images. After registering the $NB403$ and broadband images (U and B) at the sub-pixel level and matching their seeing, we construct continuum-subtracted $NB403$ images by applying the relations in Eq. (1) in 2-D. We measure the isophotal area of the emission region by running SExtractor with a threshold of $5.5 \times 10^{-18} \text{ ergs s}^{-1} \text{ cm}^{-2} \text{ arcsec}^{-2}$, which corresponds to 3σ , 1.8σ , 2.2σ , and 2.1σ above the local sky in the CDFS, CDFN, COSMOS1, and COSMOS2 fields, respectively. This measurement threshold is $\sim 2.5 \times$ higher than that adopted by Matsuda et al. (2004). However, because our survey redshift ($z = 2.3$) is lower than theirs ($z = 3.1$), we gain a factor of ~ 2.4 in surface brightness, thus achieving equivalent surface brightness ($8.6 \times 10^5 L_{\odot} \text{ kpc}^{-2}$ compared to their $8.2 \times 10^5 L_{\odot} \text{ kpc}^{-2}$). We also estimate local sky background using a fairly large background mesh size ($\sim 60'' \times 60''$), so as not to mistakenly subtract the extended $\text{Ly}\alpha$ emission as a local background.

Measuring the size of a low surface brightness feature is always subject to the noise and filtering. After testing the various smoothing filters in SExtractor, we adopt a 5×5 pixel² Gaussian kernel with FWHM = 2 pixels to compromise between signal-to-noise (S/N) and over-smoothing. We choose this truncated smoothing kernel such that it can enhance S/N in the low surface brightness wings while not spreading the bright core into the outer part. We note that the measured isophotal area depends strongly on the choice of the filters and recommend specifying the smoothing kernel and detection threshold when reporting blob size to allow a direct comparison between different samples. Appendix A shows what sizes and fluxes the 35 blobs from Matsuda et al. (2004) would have if those blobs were measured following our procedures. In our survey, the Matsuda et al. (2004) blobs

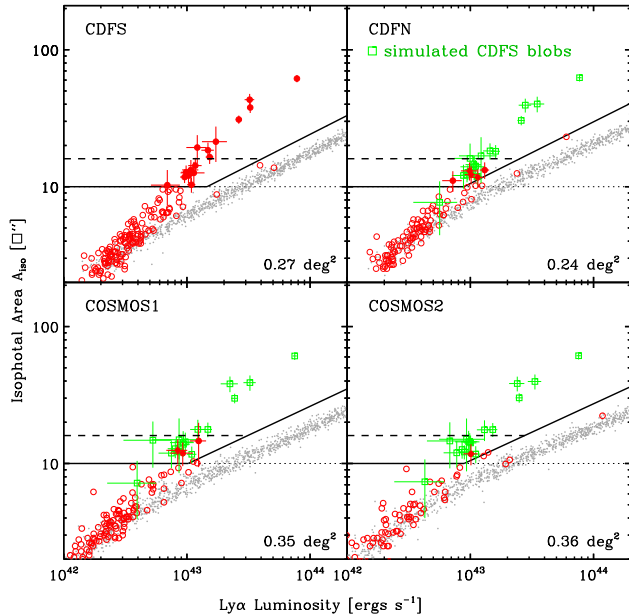


FIG. 4.— Distribution of isophotal areas (A_{iso}) and Ly α luminosities of Ly α -emitting sources (red circles) in the CDFS, CDFN, and two COSMOS subfields. Thick solid lines represent the selection criteria for the final Ly α blob candidates: $A_{\text{iso}} > 10 \square''$ and distinguishable from point sources, i.e., deviating from the simulated point source locus of small grey dots by $> 4\sigma$. Simulated point sources mix with extended Ly α -emitting sources below our selection limits in A_{iso} and $L_{\text{Ly}\alpha}$, making it difficult to distinguish blobs from point sources there. The horizontal dashed line represents the division ($A_{\text{iso}} = 16 \square''$) between the brightest, largest blobs and the other blob candidates. The former are discovered only in the CDFS. The green squares in the CDFN, COSMOS1, and COSMOS2 panels represent the A_{iso} and $L_{\text{Ly}\alpha}$ that the 16 CDFS blobs would have if they were observed at the seeing and depth of each of the other fields (see §4.3). The six brightest, largest blobs ($L_{\text{Ly}\alpha} \gtrsim 1.5 \times 10^{43}$ ergs s $^{-1}$ and $A_{\text{iso}} > 16 \square''$) in the CDFS should have been detected in the other fields. Therefore, we conclude that the observed strong field-to-field variation is real and not due to observational biases (see §4.3).

would be smaller, and the smallest blobs would have an isophotal area of $A_{\text{iso}} \sim 10 \square''$. Therefore, we adopt this value as the size lower-bound when selecting our blob sample.

One of the potential problems in detecting a blob is contamination by point sources. To quantify this effect, we place artificial point-sources with a range of luminosities ($L_{\text{Ly}\alpha} = 10^{42} - 10^{45}$ ergs s $^{-1}$) into the sky regions and measure their sizes and fluxes in the same manner as for the extended sources. We then determine the isophotal area versus luminosity limits above which extended and point sources can be differentiated.

Figure 4 shows the distribution of the angular sizes and line luminosities of the Ly α -emitting blob candidates assuming that they are all at $z = 2.3$. The open and filled circles represent the line-emitting objects selected using our line-emission criteria (Fig. 3), and the gray dots show the relation between size and brightness for the artificial point sources. To choose the final blob candidates, we select objects with isophotal areas larger than $10 \square''$ that lie more than 4σ above the $L_{\text{Ly}\alpha}$ - A_{iso} relation defined by the point sources. Below these limits, extended and point sources mix, and the sizes of blobs cannot be measured reliably, as explained below.

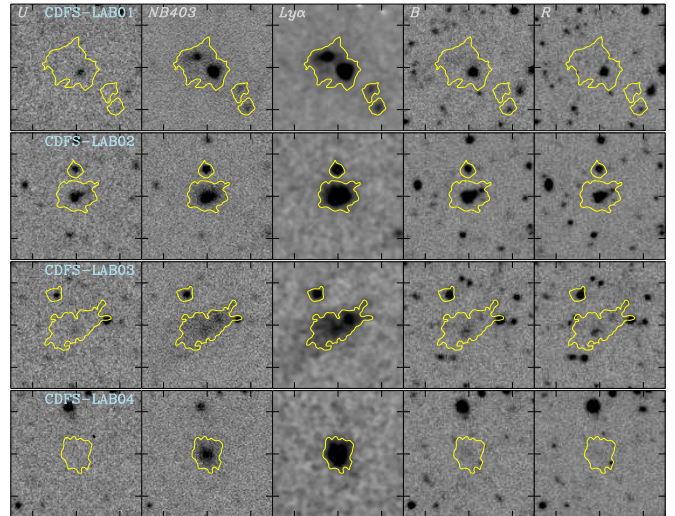


FIG. 5.— Cut-out images of the 16 Ly α blobs that we discover in the Extended CDFS. Images from left to right: U , NB403, continuum-subtracted Ly α line ($\lambda_c \simeq 4030\text{\AA}$), B , and R band. The ticks are spaced in $10''$ intervals. The overlaid (yellow) contours represent a Ly α surface brightness of 4×10^{-18} ergs s $^{-1}$ cm $^{-2}$ arcsec $^{-2}$, our 2.2σ detection limit in the narrowband images. In each case, the Ly α emission is more extended than the broadband counterpart. All five candidates that we have now observed spectroscopically are confirmed as blobs at $z = 2.3$ (Yang et al., in prep.).

Because the chosen isophotal threshold is comparable to the rms sky noise ($1.8\sigma - 3\sigma$ depending on the field), we test how reliably we can measure the spatial extent of the blob candidates. We cut a small (101×101 pixel 2) section around each candidate from the line-only image, filter it with a smoothing kernel,⁹ place each postage stamp into ~ 1000 empty sky regions, and extract the sources with SExtractor in the same way as for the real data. Then we check how often and accurately the blob sizes are recovered from these simulated images. The recovery fraction (f_{recv}) represents how frequently an artificial blob is recovered with a size larger than $10 \square''$. The size error becomes comparable to the measured size below our sample selection limits, and f_{recv} drops from $\gtrsim 90\%$ to $\sim 50\%$ at the selection boundary for the brightest blob candidates.

Our “blob” definition requires their Ly α emission to be more spatially extended than their stellar continuum emission. Thus, their extended light represents the intergalactic medium instead of the galaxies. Our choice of size cut is not due to any discontinuity, and is limited only by the ground-based seeing. Therefore, higher spatial resolution images would likely detect fainter or more compact blobs. Stacked images of LBGs (Lyman Break Galaxies) do reveal faint extended emission (Hayashino et al. 2004).

4. RESULTS

4.1. Discovery of Ly α Blobs

The total area of our survey is ~ 1.2 deg 2 . Our Ly α blob (LAB) selection criteria, $\text{EW}_{\text{obs}} > 100 \text{\AA}$ and $A_{\text{iso}} > 10 \square''$ above the surface brightness threshold of 5.5×10^{-18} ergs s $^{-1}$ cm $^{-2}$ arcsec $^{-2}$, yield a total of 16, 5, 3,

¹⁰ We use a 5×5 pixel 2 convolution mask with FWHM = 2 pixel.

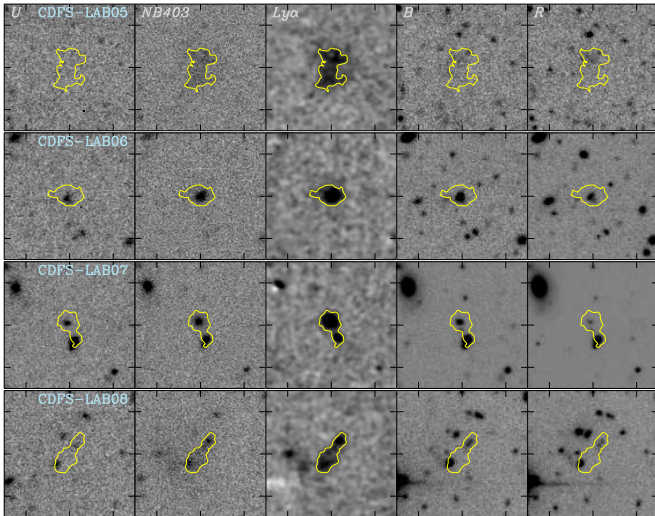


FIG. 5.— Continued.

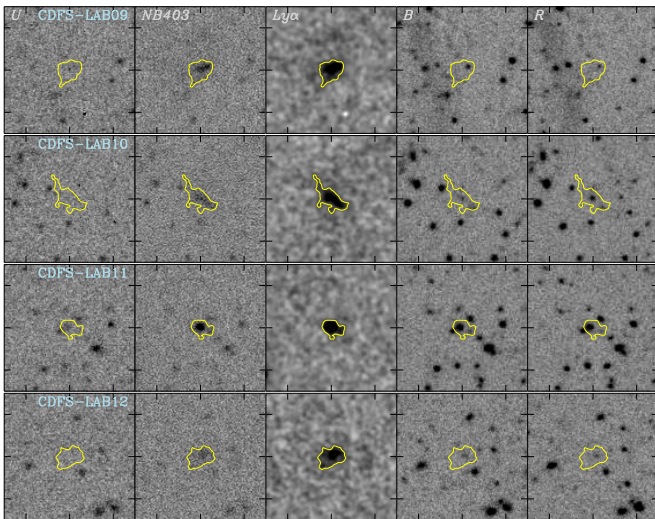


FIG. 5.— Continued.

and 1 blob candidates in the CDFS, CDFN, COSMOS1, and COSMOS2 fields, respectively. We list their basic properties in Table 3: coordinates, $\text{Ly}\alpha$ luminosity, and isophotal area.

Figures 5–7 show postage-stamp images of all 25 blob candidates in the NB403 band, continuum-subtracted $\text{Ly}\alpha$ line emission, and three broadbands (UBR) overlaid with the $\text{Ly}\alpha$ contour corresponding to a surface brightness of $4 \times 10^{-18} \text{ erg s}^{-1} \text{ cm}^{-2} \text{ arcsec}^{-2}$.

Although we select blob candidates quantitatively, follow-up visual inspection indicates that the spatial extents of four blobs are not clearly larger than the local PSF: CDFN-LAB02, CDFN-LAB03, COSMOS-LAB01, and COSMOS-LAB02. Therefore, we flag them as “marginal”. Excluding them does not affect our conclusion regarding the large field-to-field variation in the blob number density and, in fact, makes that case stronger. The largest blobs (more than $16 \square''$; the dashed line in Fig. 4) are the most robustly extended and are

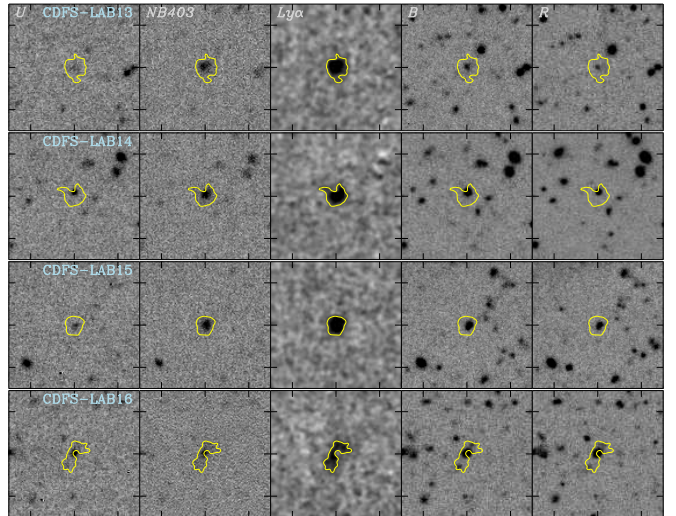


FIG. 5.— Continued.

comparable to those identified in other surveys (e.g., Matsuda et al. 2004). Therefore, we treat them separately as the “bright/large” subset of the entire blob sample in the clustering analysis in §4.3.

The blob candidates have a wide range of sizes and line luminosities: $A_{\text{iso}} = 10 \square'' - 60 \square''$ and $L_{\text{Ly}\alpha} = 0.7 - 8 \times 10^{43} \text{ erg s}^{-1}$. They show diverse morphologies ranging from compact (the south-west clump of CDFS-LAB01) to diffuse (CDFS-LAB05) to highly elongated (CDFS-LAB08 and 16). We do not find any bubble-like structures that might be associated with superwinds like those in a few of the blobs identified by Matsuda et al. (2004).

We are following up the entire blob sample spectroscopically. To date, we have observed five blobs (CDFS-LAB01, 02, 04, 10, 14) of the 16 in the CDFS. We confirm all five spectroscopically with their $\text{Ly}\alpha$ and/or $\text{H}\alpha$ lines. The details of our spectroscopic campaigns are presented in a forthcoming paper (Yang et al., in prep.).

The properties of continuum objects associated with blobs provide valuable clues to the source of blob emission (Yang et al., in prep.). For example, the blob discovered in the CDFS at $z = 3.1$ by Nilsson et al. (2006) is not associated with any continuum source within $\sim 3''$ (but see also Geach et al. 2009). Thus, it is possible that this blob is powered by cooling radiation or cold mode accretion. Although most blob candidates in our sample have clear continuum source counterparts in the rest-frame UV images, two blobs (CDFS-LAB04 and CDFS-LAB05) do not. We are, however, able to identify continuum sources within these blobs in deep, rest-frame UV HST images (GEMS and GOODS-S; Rix et al. 2004; Giavalisco et al. 2004). Preliminary inspection of the multiwavelength images also reveals bright IR or X-ray sources in these blobs. Interestingly, we often find *multiple* continuum sources in a blob, notably in LAB02 and LAB03. Our initial examination of the HST images of the 16 $\text{Ly}\alpha$ blobs in the CDFS often resolves these sources as galaxies, suggesting that star formation and/or nuclear activity might play a role in producing the $\text{Ly}\alpha$ emission (e.g., Colbert et al. 2006). This apparent clus-

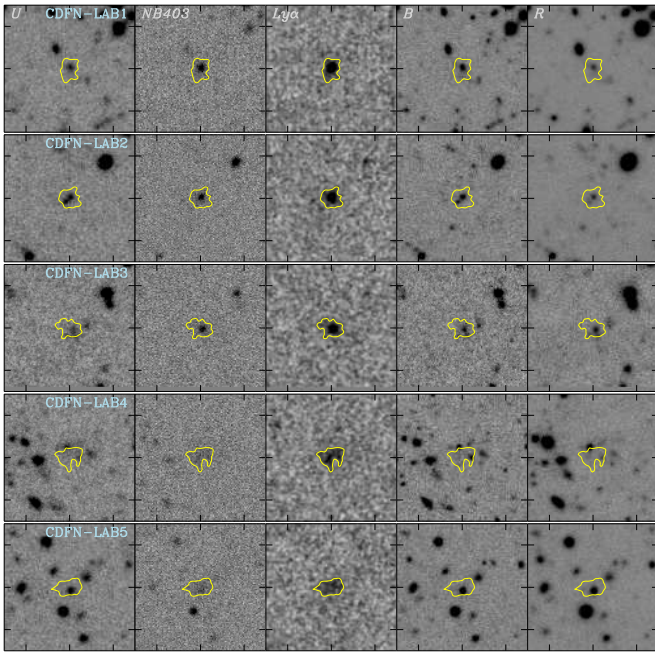


FIG. 6.— Same as Figure 5, but for the five Ly α blob candidates in the CDFN field.

tering of sources within some blobs may indicate that blobs are the progenitors of groups or clusters of galaxies today. We test this possibility quantitatively in §4.3.

4.2. Continuous LAE-to-LAB Sequence

There is no evidence of a discontinuity between the properties of our blobs and unresolved, compact Ly α emitting (LAE) galaxies (i.e., the sources below the solid lines in Fig. 4). The smoothness of the LAE-to-LAB transition, which has also been observed by Matsuda et al. (2004), suggests that these two types of Ly α sources may not be distinct and that whatever mechanism or mechanisms power blobs work over a wide range of luminosity and spatial extent. Understanding the origin of the extended Ly α emission requires us to probe the host galaxy properties — including the stellar mass, star formation rate, and size of the star-forming region — along the emitter-to-blob sequence. If extended star formation or AGN are responsible for powering the emission, we would expect that the properties of blobs (A_{iso} , $L_{\text{Ly}\alpha}$) are correlated with either star formation rate or X-ray luminosity of the host galaxies. For example, Geach et al. (2005) argue that a correlation between the Ly α and bolometric (actually FIR) luminosity (although weak) suggests that the interaction of an ambient halo of gas with a galactic-scale superwind is responsible for the majority of LABs. We discuss the multi-wavelength properties of galaxies within or near the blobs, considering them as possible energy sources, in a separate paper (Yang et al., in prep.).

4.3. Significant Differences in Blob Counts per Field

Surprisingly, most blobs (16/25) and all eight of the brightest, largest blobs ($A_{\text{iso}} > 16\text{''}$, $L_{\text{Ly}\alpha} \gtrsim 1.5 \times 10^{43}$ ergs s $^{-1}$) lie in only one of the survey fields: CDFS. Because the depth and seeing of the CDFS images are also

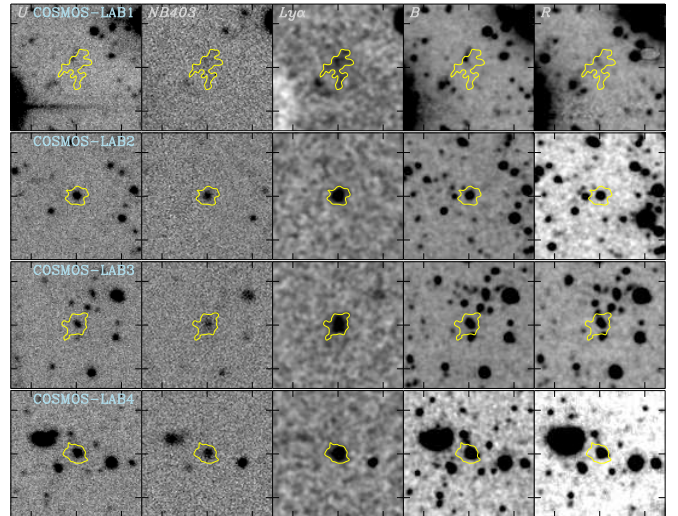


FIG. 7.— Same as Figure 5, but for the three Ly α blob candidates in the COSMOS1 subfield (top rows) and the one candidate in the COSMOS2 subfield (bottom row).

superior to the other fields, we first need to verify that this field-to-field variation of the blob number density does not arise from selection effects. For example, although the separation between the fainter/smaller blob candidates and the simulated point-sources is distinct in the CDFS, the separations in other three fields are less clear.

To confirm that the field-to-field variation of the blob population is not due to the different seeing and survey depth, we simulate how the blob candidates in the CDFS field would look if observed in the other three fields. Using the continuum-subtracted postage stamp ($27'' \times 27''$) images of the CDFS blob candidates, we first degrade their seeing to that of the CDFN, COSMOS1, and COSMOS2 fields by convolving kernels derived from PSF images. We rebin the images (if pixel scale is different), add Poisson noise, and place them into empty sky regions in the continuum-subtracted narrowband images of the other fields. We then measure the blob sizes and luminosities in the same way as described in §3. We repeat this experiment ~ 1000 times to derive the range of recovered luminosities and sizes.

We show the isophotal areas and Ly α luminosities ($A_{\text{iso}} - L_{\text{Ly}\alpha}$) from this recovery test as green squares in the CDFN, COSMOS1, and COSMOS2 panels in Figure 4. If we estimate the number of possible detections as $N = \sum_{f_{\text{recv}} > 50\%} f_{\text{recv}}$, the number of CDFS-like blobs that should have been detected as bright/large blobs with $A_{\text{iso}} > 16\text{''}$ and $L_{\text{Ly}\alpha} \gtrsim 1.5 \times 10^{43}$ ergs s $^{-1}$ is 6.9, 6.0, and 6.0, respectively, for each of the three other fields. However, we do not find such blobs in other fields, so we conclude that the observed field-to-field variation is real and that the minimum variation in the number counts of the largest blobs ($A_{\text{iso}} > 16\text{''}$) is at least $N_{\text{blob}} = (N_{\text{CDFS}}, N_{\text{CDFN}}, N_{\text{COSMOS1}}, N_{\text{COSMOS2}}) = (6, 0, 0, 0)$. Throughout the rest of this paper, we refer to this as the “bright/large blob sample” and use it as the default for analyzing blob statistics. When we lower the criteria for the blobs to $A_{\text{iso}} > 10\text{''}$, we expect 14.0, 13.9, and 13.7 blobs in the other three fields, respectively, whereas we

find 5, 3, and 1 blob candidates. In this case, the observed contrast between the four survey fields is $N_{\text{blob}} = (14, 5, 3, 1)$. We subsequently refer to this as the “entire blob sample”. We consider the bright/large sample and entire sample field-to-field variations in N_{blob} , which are corrected for the different survey conditions, in deriving the average number density and its variance in the following paragraphs. The blob statistics are summarized in Table 4.

Could this observed field-to-field variation arise solely from the statistical uncertainty? Before we proceed to a detailed analysis, we have to rule out the possibility that this result arises solely from Poisson (shot) noise. For the hypothesis that the surface density of the bright/large Ly α blob sample is 2–20 blobs deg^{-2} or $\sim 0.5 - 5$ blobs per survey field, we calculate the probability of observing non-detections in three survey fields and detections more than six blobs in any of the fields. We are able to rule out a uniform distribution with at least 99.97% confidence ($\sim 3.6\sigma$). For the entire blob sample, a uniform distribution is excluded at the 3.7σ level. In §4.3.3, we compare the observed field-to-field variations with those derived from Poisson statistics and cosmological N-body simulations, respectively. We show that the latter better reproduces the observations.

4.3.1. Quantifying Blob Field-to-Field Variance

In this section, we estimate the field-to-field variation in the number density of Ly α blobs from the observed number statistics, N_{blob} . According to Λ CDM cosmology, the number density and variance of a galaxy population are not entirely independent properties, but a function of halo mass. Here we treat them as independent parameters and aim to measure them as observables by adopting a simple analytic approximation of the underlying fluctuations in blob number density arising from large-scale structure. This method has the advantage that the blob number density and variance can be derived over a wider range of parameter space than sampled by simulations. We then compare these properties with the predictions from the simulations to obtain constraints on the halo mass (§4.3.3). As will be shown in the following section (§4.3.2), one must consider the field-to-field variations to correctly estimate the uncertainties in number density and to thus compare blob statistics across different surveys.

The simplest way of quantifying the field-to-field variation, σ_v^2 , is to adopt the relation (Peebles 1980, §36):

$$\sigma_v^2 = \frac{\langle N^2 \rangle - \langle N \rangle^2}{\langle N \rangle^2} - \frac{1}{\langle N \rangle}, \quad (2)$$

where N is the number of blobs per 0.25 deg^2 , the typical area of each of our four fields, and σ_v^2 is the fractional variance corrected for Poisson noise. The number density n can be derived directly from N by dividing it by the survey volume: $n \equiv 8.6 \times 10^{-6} N \text{ Mpc}^{-3}$. Hereafter, we use surface density to mean surface number density. Thus σ_v^2 represents the fractional uncertainty in the observational estimate due to finite survey volume. For the bright/large sample, we obtain $\langle N \rangle = 1.5$ and $\sigma_v \simeq 1.5$ (150%). For the entire blob sample, $\langle N \rangle = 5.75$ and $\sigma_v \simeq 0.76$, or 76%. Because of our small number statistics, we choose to adopt a more sophisticated method to bet-

ter understand the possible range of blob number density and its variance.

To quantify the field-to-field variance of the blob population, we calculate the posterior probability for σ_v^2 and an average surface density per 0.25 deg^2 (\bar{N}) given our observation (D) of (6, 0, 0, 0) blobs in the bright/large sample:

$$p(\sigma_v, \bar{N}|D) \propto \text{prob}(D|\sigma_v, \bar{N}) p(\sigma_v, \bar{N}). \quad (3)$$

First, we assume that the field-to-field variance follows the log-normal distribution: $(N/\bar{N}) \sim \text{Log-N}(0, \sigma_{\text{LN}}^2)$; in other words, $\log(N/\bar{N})$ follows a normal distribution $N(0, \sigma_{\text{LN}}^2)$. Here, σ_{LN}^2 is the variance of the log-normal distribution and is related to the actual variance by $\sigma_v^2 = \exp(\sigma_{\text{LN}}^2) - 1$. Unlike a Gaussian distribution, the log-normal distribution does not allow negative values for N and naturally introduces a skewness into the distribution. When $\sigma_v \ll 1$, the log-normal distribution is similar to Gaussian, but the distribution becomes skewed toward zero as σ_v increases, effectively mimicking the dark matter fluctuations at the high mass end (Coles & Jones 1991; Bernardeau & Kofman 1995). We choose the log-normal distribution for the simplicity here, but any reasonable functional form capable of representing this skewness can be used.

Second, for a given set of (σ_v, \bar{N}) , we calculate the probability, $\text{prob}(D|\sigma_v, \bar{N})$, of finding six blobs in one field and none in three other fields assuming that the observed number of blobs follows Poisson statistics with a mean of \bar{N} . We adopt logarithmic priors for both σ_v and \bar{N} , which indicates $p(\sigma_v) \propto 1/\sigma_v$ or $p(\bar{N}) \propto 1/\bar{N}$, implying that the *scale* of \bar{N} and σ_v is unknown, i.e., that the priors are uniform in logarithmic bins. We consider a range of $0.1 < \bar{N} < 30$ and $0.1 < \sigma_v < 10$, i.e., 10% to 1000% field-to-field variance. We also test other priors including (1) a linear prior for both σ_v and \bar{N} and (2) a logarithmic prior for σ_v and linear prior for \bar{N} , but the choice of prior does not affect our conclusions.

Figure 8 shows the posterior probability distribution of the average surface density and variance for the bright/large blob sample (*left*) and the entire sample (*right*). For the bright/large blobs, the posterior favors high variance ($\sigma_v \gg 1$) as expected. The confidence regions are not closed, allowing us to put only a lower bound on σ_v . The lower limits are $\sigma_v > 1.45$ and $\sigma_v > 0.57$ for the 1σ and 2σ confidence levels, respectively, for the joint distribution (i.e., we attempt to constrain both \bar{N} and σ_v at the same time). The 1σ , 2σ and 3σ confidence regions are determined such that the corresponding contours enclose 68.3%, 95.5%, and 99.7% of total posterior probability. The 3σ lower limits are not constrained because the priors become too high as $\sigma_v \rightarrow 0$, thus the posterior probability is determined more by the input priors rather than by the data themselves.

We also calculate the confidence interval for each parameter (σ_v or \bar{N}) by marginalizing out the other parameter in the posterior probability distribution: e.g., $p(\bar{N}|D) = \int p(\sigma_v, \bar{N}|D) d\sigma_v$. This interval then represents the estimate of one parameter independent of the other. In §4.3.2, we compare the marginalized surface density estimates, *regardless of the variance*, with those obtained from past observational studies. In Table 5, we show the blob surface density (\bar{N}) and variance esti-

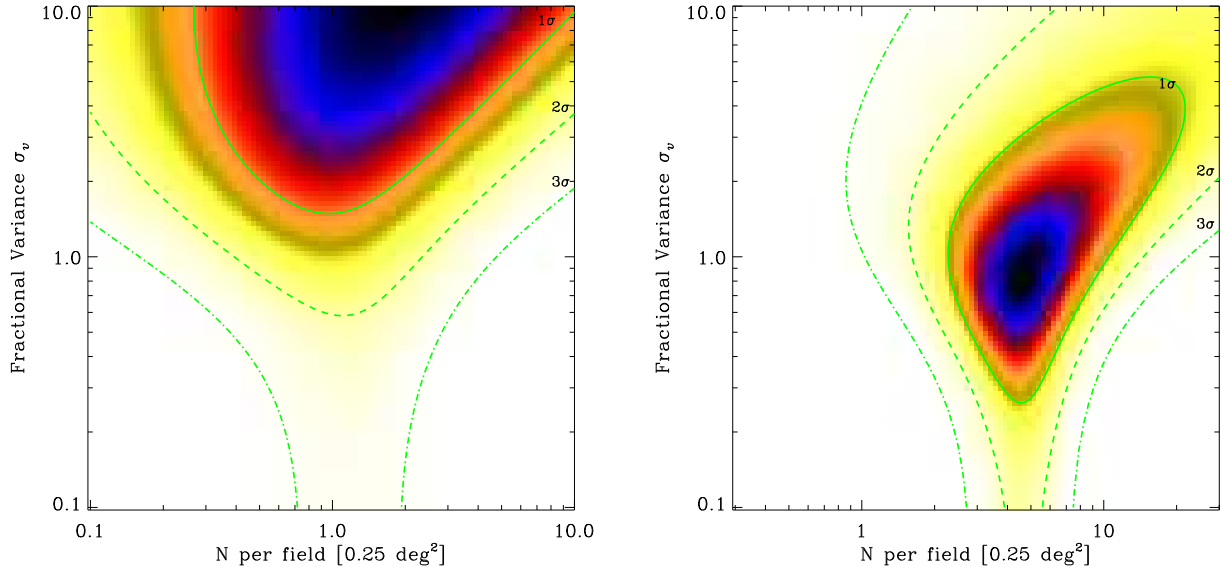


FIG. 8.— Posterior probability distribution of the fractional variance (σ_v) and the average surface density per field (\bar{N}) for the bright, large blobs (*left*) and the entire blob sample (*right*). We adopt logarithmic priors for both σ_v and \bar{N} . The 1σ , 2σ and 3σ confidence regions are determined such that the corresponding contours enclose 68.3%, 95.5%, and 99.7% of the total posterior probability. The bright, large blobs have fractional variances of at least 1.5 (150%) at 1σ and 0.6 (60%) at 2σ regardless of the estimated number density, confirming that blobs are highly clustered. For the entire blob survey, the most probable estimate is $(\bar{N}, \sigma_v) \simeq (4.8, 0.9)$.

mates obtained from the above. The field-to-field variation of the bright/large blobs is stronger than 150% and 60% at the 1σ and 2σ confidence levels, respectively. For the entire blob sample, the most probable parameters are $(\bar{N}, \sigma_v) \simeq (4.8, 0.9)$ with large uncertainties of $0.26 < \sigma_v < 5.2$ at the 1σ level. The large variance implies a highly skewed distribution and thus reproduces the observed strong field-to-field variations.

Observationally, $\sigma_v \sim 1.5$ (150%) is much larger than for compact Ly α emitters (LAEs) at $z = 3$ –5 obtained from narrowband imaging over volumes comparable to our survey. For example, we estimate a LAE variance of ~ 20 –30% at $z \approx 3.1$ from the five 0.2 deg^2 subfields of Ouchi et al. (2008). From Shioya et al. (2009), we estimate that the LAE variance at $z \approx 4.86$ is likewise $\sim 30\%$ when their contiguous survey area ($\sim 2 \text{ deg}^2$) is divided into 0.25 deg^2 subfields (their Table 2). This $\sim 30\%$ variance is enough to produce the factor of 2 difference among the LAE number densities observed in their fields. Note that the $\sim 30\%$ LAE variance is uncorrected for Poisson noise, which would lower it. Therefore, the even larger variance of blobs suggests that they lie in halos more massive than those of LAEs. We put the first constraints on the dark matter halo mass of blobs in §4.3.3 by comparing our blob statistics with N-body simulations.

The strong variation in blob counts from one 0.25 deg^2 field to another is consistent with the discovery of a close pair of blobs by Yang et al. (2009). Those blobs were among only four detected in our shallower, but larger (4.8 deg^2) survey of the NOAO Boötes field. They are separated by only $\sim 70''$. If that survey had been conducted by mosaicing $30' \times 30'$ fields like those sampled by our imager here, most fields would not contain the pair. On a related note, the clustering of 35 blobs in the SSA22 overdensity (Matsuda et al. 2004) was identified during a follow-up of two giant blobs originally found by

Steidel et al. (2000).

4.3.2. Blob Number Density and Luminosity Function

The strong field-to-field variation of the Ly α blobs presents challenges for the measurement of their number density and luminosity function (LF). In this section, we compare our LFs derived from each survey field with each other and with previous studies. We demonstrate that a large volume survey and/or multiple pointings are critical to constrain the blob LF. For the rest of paper, we adopt the marginalized number densities from the previous section, which give us the number densities of $n = 1.0_{-0.6}^{+1.8} \times 10^{-5} \text{ Mpc}^{-3}$ (from $N = 1.2$ per 0.25 deg^2) for the bright/large blob sample and $n = 4.1_{-1.6}^{+4.8} \times 10^{-5} \text{ Mpc}^{-3}$ (from $N = 4.8$ per 0.25 deg^2) for the entire blob sample.

First, we compare the number density of bright/large blobs derived from §4.3.1 with previous measurements (Figure 9). To make a fair comparison with other work, we need to cut the bright/large sample to satisfy the selection criteria used by Yang et al. (2009) when they previously examined the blob number densities among different samples spanning $z = 0.8$ to 6.6. Those criteria were: $L_{\text{Ly}\alpha} > 1.5 \times 10^{43} \text{ ergs s}^{-1}$ and $A_{\text{iso}} > 25 \square''$ above a surface brightness threshold of $5 \times 10^{-18} \text{ ergs s}^{-1} \text{ cm}^{-2} \text{ arcsec}^{-2}$ under $\sim 1.8''$ seeing. We refer readers to Yang et al. (2009) for the details about the estimates at each redshift.

Only four blobs (CDFs-LAB01, 02, 03, and 04) from the sample of six bright/large blobs satisfy the Yang et al. (2009) criteria, so we scale the bright/large counts down by a factor of 4/6, obtaining a surface density of $0.77_{-0.5}^{+1.4}$ per 0.25 deg^2 fields or a number density of $n = 0.66_{-0.4}^{+1.2} \times 10^{-5} \text{ Mpc}^{-3}$ (*large, open square* in Fig. 9). The error bar takes into account the field-to-field variation as well as the Poisson noise. This average

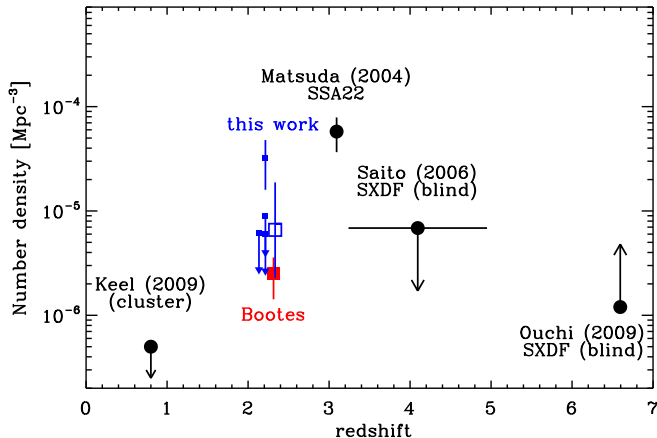


FIG. 9.— Number density of Ly α blobs at different redshifts. The filled and open squares are from our two narrow-band imaging surveys at $z = 2.3$: the ultra-wide Bok+90Prime survey in Boötes (Yang et al. 2009) and the narrower, but deeper, NOAO-4m survey (this work), respectively. The filled dots are the number density estimates from Matsuda et al. (2004); Saito et al. (2006); Ouchi et al. (2009); Keel et al. (2009). All the number densities plotted here are scaled to match the shallowest survey (Boötes field) with $\sim 1.8''$ seeing and an rms sky background of 5×10^{-18} ergs s $^{-1}$ cm $^{-2}$ arcsec $^{-2}$. The upper or lower limits on several of the points from the literature are explained in Yang et al. (2009). The four small squares represent the individual number density estimates for each of our four survey fields, demonstrating that a large volume survey is required to overcome the strong field-to-field variation of the blobs. Note that these data points are shown slightly shifted for clarity, but they are all at $z = 2.3$.

number density at $z = 2.3$ derived from the four NOAO-4m survey fields is thus consistent with the Yang et al. (2009) measurement at the same redshift ($n = 0.25 \pm 0.10 \times 10^{-5}$ Mpc $^{-3}$; *large, filled square*) obtained from our $\sim 4 \times$ larger volume survey of Boötes.

To illustrate the uncertainties arising from the field-to-field variance, we show the bright/large number density for each of the four fields individually. The small squares represent $n = 3.2 (\pm 1.6) \times 10^{-5}$ Mpc $^{-3}$ for the CDFS, and three upper limits, $n < 0.90, 0.62, 0.60 \times 10^{-5}$ Mpc $^{-3}$ for CDFN, COSMOS1, and COSMOS2, respectively. The number density in the CDFS field is consistent with that found by Matsuda et al. (2004) in the SSA22 field ($5.8 \pm 2.1 \times 10^{-5}$) within the uncertainties, suggesting that blobs at $z = 2.3$ in the CDFS also lie in an overdense region (see also Palunas et al. 2004; Prescott et al. 2008) and occupy high mass halos. On the other hand, the blob number densities for the other three fields are lower than for the CDFS and the SSA22 field, demonstrating that characterizing the evolution in n with z requires surveys large enough to overcome the field-to-field variance. Because such measurements are not yet available at other redshifts, it is not possible to constrain $n(z)$ at this time.

Note that we are not able to apply the Yang et al. (2009) selection criteria to the higher- z Saito et al. (2006) and Ouchi et al. (2009) blob samples because those authors use selection methods different than ours and Matsuda et al. (2004). Therefore, we plot these higher- z estimates as upper and lower limits, respectively. Unlike the comparison between the $z = 2.3$ and $z = 3.1$ samples, comparison of the Saito et al. (2006) and Ouchi et al. (2009) points with our results is per-

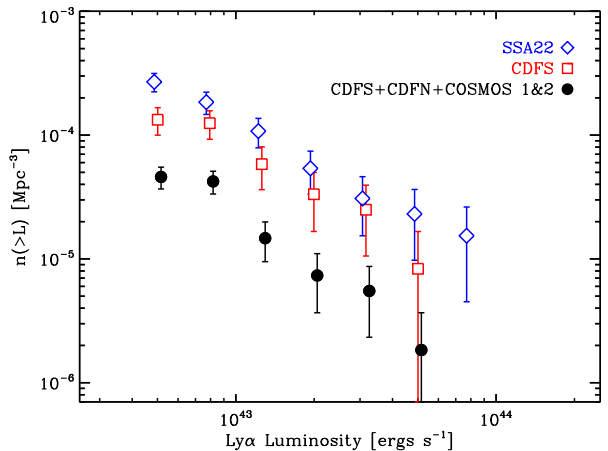


FIG. 10.— Cumulative Ly α luminosity function (LF) for Ly α blobs. The open squares (red) and diamonds (blue) represent the LFs derived from the CDFS (this paper) and SSA22 (Matsuda et al. 2004) fields, respectively, which each have a survey area of ~ 0.25 deg 2 . The filled dots represent the average LF measured from all four of our survey fields (CDFS, CDFN, COSMOS1, and COSMOS2). Data points are slightly shifted relatively to each other for clarity. While the slope and normalization of the CDFS and SSA22 LFs roughly agree, the normalization of the average LF is \sim four times lower, suggesting that one should account for the strong field-to-field variation of Ly α blobs when calculating LFs.

ilous. We plot all these points together only to summarize the state of blob surveys.

In addition to the blob statistics obtained from narrow- or intermediate-band imaging techniques, we show the number density estimate ($n < 0.5 \times 10^{-6}$ Mpc $^{-3}$) from GALEX slitless spectroscopy of two galaxy (super)clusters at $z \simeq 0.82$ (Keel et al. 2009). This n , even though calculated from overdense regions, is well below that of the overdense CDFS and Matsuda et al. (2004) fields, supporting the Keel et al. (2009) claim that Ly α blobs might be high redshift phenomena. Additional surveys at $z < 1$ are required to confirm this result, as we do not know whether the variance in n at $z = 2.3$ persists at lower z .

Second, we compare our blob luminosity function with that of Matsuda et al. (2004) in Figure 10. The similar depth and selection criteria of the two surveys makes the direct comparison meaningful (see Appendix A). For each of our blobs, we use the *total* Ly α luminosity (Table 3), which our recovery test demonstrates is reliable. The isophotal flux could be biased due to the different signal-to-noise and filtering kernels used in the detection procedure. We construct an average LF as follows. In each Ly α luminosity bin, we divide the number of blobs found in all four of our survey fields by the total survey volume. We also plot the LF obtained from only the 16 blobs in the CDFS. We do not apply a completeness correction using the recovery fraction f_{recv} in Table 3, because we also do not know the completeness of Matsuda et al. (2004) sample. In Table 6, we list our blind survey LFs as well as that of the SSA22 overdense region (Matsuda et al. 2004).

The slope and normalization of the CDFS (squares) and Matsuda et al. (2004) (diamonds) LFs agree roughly. The apparent discrepancy in the faintest bin ($\log L_{\text{Ly}\alpha} = 42.8$) is likely due to incompleteness in our survey. We

also do not find any blobs as bright as those in their brightest bin ($\log L_{\text{Ly}\alpha} = 44.0$). Not surprisingly, the normalization of our “average” luminosity function (filled circles) is $\sim 4\times$ lower than those of the CDFS and Matsuda et al. (2004) LFs. Once again, we see that comparisons among surveys are difficult without knowledge of the blob clustering strength and that large volume surveys are required to overcome the strong field-to-field variance of the blob counts. The same conclusion is reached from the on-going Subaru survey of blobs (see Fig. 13 of Goerdt et al. 2009, Y. Matsuda in preparation).

The clustering of blobs provides a means to discriminate among models for the origin of the extended Ly α emission, including photoionization by AGN, outflows due to intense star formation, and cooling radiation. This analysis is beyond the scope of this paper, but we note that any blob-producing mechanism must reproduce both the observed LF and its field-to-field variation. For example, it would be interesting to ascertain whether AGN or sub-millimeter galaxies (SMGs) have clustering strengths similar to blobs. Along these lines, Dijkstra & Loeb (2009) claim that Ly α blobs are cooling radiation arising from cold streams falling onto the embedded galaxies and that a strong variance naturally arises from the underlying variation of dark matter halos (see also Goerdt et al. 2009).

4.3.3. Blob Halo Masses

Because our blob survey is blind and sufficiently large to determine the blob number density and its variance, we have a unique opportunity to constrain the properties of the dark halos in which the blobs reside, and thus to understand what these mysterious objects have evolved into today. For example, based on the blob number density and the discovery of the blob pair in the NOAO Deep-Wide Boötes field, Yang et al. (2009) suggest that blobs are sites for the formation of the brightest galaxies in rich galaxy clusters. However, the small number statistics of that study precluded constraining the mass of blob halos. Although our current survey statistics are still not large enough to directly measure the clustering of blobs via correlation function analysis, we can use n , σ_v , and a cosmological N-body simulation of Λ CDM universe to identify the most likely halo mass occupied by blobs.

We first select a dark halo (DM) mass in which blobs could reside. All halos above this minimum mass M_{min} have a fixed probability of containing a detectable blob, which is labeled the detectability fraction f_{D} ¹¹. We choose f_{D} such that the halo mass function from the simulation reproduces the observed blob number density from §4.3.1. Once the halo mass and detectability fraction are fixed, we can predict the clustering of such halos, i.e., the field-to-field variation, directly from the simulation using counts-in-cells (c-in-c) methodology. Then we compare this prediction to the observed variation in blob counts over the four survey fields to quantify the likelihood that the selected halo mass and detectability fraction reproduce the observed blob statistics in Table

4.

To link the number density and its variance to the DM halo mass, we employ a simple counts-in-cells analysis using the halo catalog at $z = 2$ derived from the ABA-CUS N-body code (Metchnik & Pinto, in prep.). This simulation has a cubic volume of $1h^{-1}$ co-moving Gpc on a side and 1024^3 dark matter particles with $m_{\text{DM}} = 1.1\times 10^{11} M_{\odot}$. We adopt the cosmological parameters: $H_0 = 0.701$, $n_s = 0.96$, $\Omega_{\text{M}} = 0.279$, $\Omega_b = 0.0456$ and $\sigma_8 = 0.817$. Dark halos are defined using a friends-of-friends algorithm with linking length $b = 0.16$ in units of the initial particle spacing. The smallest halos used in our analysis consist of 48 particles. Due its large size, this simulation is finely tuned to our problem, which requires sampling many “cells,” ~ 50 comoving Mpc boxes that are roughly the same size and geometry as our survey of each of the four fields.

To constrain the DM halo mass of the blobs, we first consider the observed bright/large blob number density $N = 1.2$ per 0.25 deg^2 field, or $n = 1.0\times 10^{-5} \text{ Mpc}^{-3}$ (1.5 blobs in a 50 Mpc box). If all halos contain a detectable blob (i.e., the detectability fraction f_{D} is 100%), then this number density requires halos with more than 150 DM particles or $1.7\times 10^{13} M_{\odot}$. We derive the counts-in-cells distribution of the simulated blobs by counting the number of blobs within 10000 randomly placed 50 Mpc boxes and by assuming a simple halo occupancy distribution (e.g., Berlind & Weinberg 2002) with $N_g(M \geq M_{\text{min}}) = 1 + (M/M_1)^\alpha$, where $M_{\text{min}} = 150$ DM particles or $1.7\times 10^{13} M_{\odot}$, $M_1 = 1000$ DM particles or $1.1\times 10^{14} M_{\odot}$, and $\alpha = 1$ as a fiducial value. This cell size is similar to our survey volume, $48.7\times 48.7\times 46.8$ Mpc, for the 0.25 deg^2 FOV with the NB403 narrowband filter. While the four survey fields have slightly different survey dimensions, the choice of a 50 Mpc box does not affect our conclusions.

Figure 11 shows the simulated bright/large blob counts-in-cells distribution with an average of 1.46 blobs per cell. The overlaid line represents a Poisson distribution with the same average, a reference case in which the DM halos containing blobs are not clustered. Thus, comparing the bright/large and Poisson distributions tests the null hypothesis that the halos and blobs are not correlated.

As expected from the large field-to-field variation (§4.3.1), the low and high tails of the simulated distribution exceed the Poisson counts. Using the Eq. (2), we derive the variance of this distribution, $\sigma_v = 1.04$, which is consistent with our estimate ($\sim 1.4\sigma$ lower limit) from the previous section (§4.3.1). This variance corresponds to a bias of $b = \sigma_{\text{blob}}/\sigma_{\text{DM}} \sim 7$ given the rms fluctuation of mass ($\sigma_{\text{DM}} = 0.15$) within a sphere of 31 Mpc radius with the same volume as our survey box.

Is this simulated distribution consistent with the observed field-to-field variation in n ? For $f_{\text{D}} = 100\%$ (shaded histogram), the probability of finding no blobs in a cell is as high as 41.5% ($\sim 2\times$ greater than the Poisson probability), while the probability of finding 6 or more blobs is 4.4% ($\sim 11\times$ greater than Poisson). The posterior probability of finding at least six blobs in one survey field with non-detections in three other fields (the case for the bright/large blobs in our sample) is 1.3% ($4 \times 0.415^3 \times 0.044$). This posterior probability is ~ 65 times larger

¹² Note that f_{D} is a statement about the detectability of the ensemble of halos and is *not* the classically-defined duty-cycle, which is simply the fraction of time a blob is on.

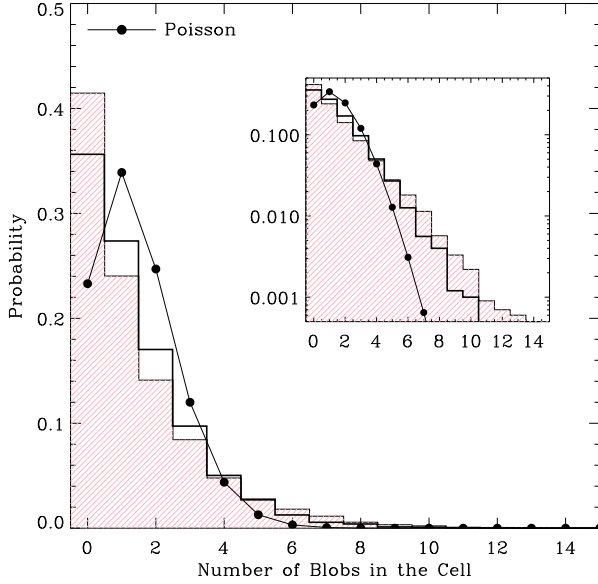


FIG. 11.— Counts-in-cells distribution of blobs drawn from the ABACUS 1 h^{-1} Gpc N-body simulation (Metchnik & Pinto, in prep.) (shaded histogram) that have the same average number density as our bright, large blob sample ($n = 1.0 \times 10^{-5} \text{ Mpc}^{-3}$). We count the number of blobs within 10000 randomly placed 50 Mpc boxes assuming that all massive halos of at least $M_{\text{min}} = 1.7 \times 10^{13} M_{\odot}$ have detectable blobs (i.e., the detectability fraction is 100%). The simulated distribution has a Poisson-noise corrected variance $\sigma_v = 1.04$, consistent with our estimates from §4.3.1. The thick solid histogram represents the distribution for a detectability fraction of 12.5% and a blob halo mass of $M_{\text{min}} = 0.5 \times 10^{13} M_{\odot}$. The observed number density and the strong field-to-field variation of the bright, large blobs at $z = 2.3$ suggest that they reside in halos that are likely to evolve into the $\sim 10^{14} M_{\odot}$ halos typical of present-day clusters of galaxies. The dots represent the Poisson noise with a mean of 1.46. The inset shows the same distribution but for a logarithmic scale.

than 0.02% for the Poisson distribution. Therefore, we reject the null hypothesis that the dark matter halos and blobs are uncorrelated.

Although the posterior probability is much higher than Poisson, is it statistically acceptable as a halo mass constraint? To test if we can reject the posterior probability of 1.3%, we consider an extreme case that maximizes our posterior statistics: $P = 4p^3(1-p)$, the probability of not finding any blob in three survey fields, but finding any number of blobs in the one remaining field. Here, p represents the probability of finding zero blobs in one survey field, and P has a maximum value of 42.2% when $p = 0.75$. Therefore, we should compare our posterior probability of 1.3% with this extreme case, not with 100%. The posterior probability is only $\sim 34\times$ smaller than this *maximum* probability. Therefore, we conclude that our measurements are consistent with the halo model assuming $M_{\text{halo}} \sim 10^{13} M_{\odot}$ and $f_D = 100\%$.

We have now established that the observed strong field-to-field variation in blob counts is not surprising if massive dark matter halos with $M_{\text{halo}} \gtrsim 10^{13} M_{\odot}$ always produce detectable Ly α blobs. Here we investigate whether it is possible to obtain consistency with lower values of halo mass by changing the blob detectability fraction. We derived the *maximal* halo mass for the observed blob number density by assuming that all halos more massive than $M_{\text{halo}} \sim 1.7 \times 10^{13} M_{\odot}$ have detectable blobs. If we

lower f_D to 50%, 25%, and 12.5%, while increasing the number density of halos capable of hosting blobs by 2, 4, and 8 times to keep the abundance of the observed blobs constant, the threshold halo mass M_{min} decreases to 1.2, 0.8, and $0.5 \times 10^{13} M_{\odot}$, respectively. At lower halo mass, we naturally obtain a weaker field-to-field variation and a less prominent high-end tail in the counts-in-cells distribution (i.e., at $N > 6$) than for $f_D = 100\%$. To illustrate this trend, we also show the counts-in-cells distributions for $f_D = 12.5\%$ (thick solid line) in Figure 11. Table 7 summarizes the counts-in-cells statistics, the field-to-field variance (σ_v), and the posterior probability of observing 6 or more blobs in only one of the survey fields for the different f_D values. For comparison, we also list the counts-in-cells statistics and the posterior probabilities for the Poisson distributions.

Higher detectability fractions (and more massive halos) produce a field-to-field variance about the observed n that is more consistent with the observed variance. Halo models with $\gtrsim 10^{13} M_{\odot}$ halos and $f_D \gtrsim 50\%$ work best. Lower detectability fractions (e.g., $\sim 12\%$) require somewhat lower halo masses ($\sim 5 \times 10^{12} M_{\odot}$) to reproduce n , but the resulting variance in n is lower and further from the observed value. However, the effects of lowering the detectability fraction and halo mass are not large enough to put strict lower limits on the halo mass: for the lowest f_D considered, 12.5%, we predict $\sigma_v = 0.76$ (76%) and a posterior probability of 0.45%, which is only $\sim 3\times$ lower than in the $f_D = 100\%$ case. It is possible, but less likely, that the blobs occupy a few $\times 10^{12} M_{\odot}$ halos if f_D is much lower than 12.5%.

A detectability fraction of $f_D = 12.5\%$ implies a short blob lifetime, only $\tau \lesssim 350$ Myrs at $z = 2-3$. In principle, we could adopt still lower values ($f_D \ll 10\%$), down to the limit where the Ly α blobs live only a few tens of Myrs, and thus lower halo masses ($\lesssim 10^{12} M_{\odot}$), in order to find the point at which we can reject the assumed halo mass. However, the limited mass resolution of our N-body code does not allow us to resolve smaller halos. Therefore, to put tighter constraints on the halo mass requires improving the blob statistics by extending surveys to larger volumes and/or creating higher resolution simulations.

For now, we conclude that bright/large Ly α blobs are most likely to reside in massive dark halos with $\gtrsim 10^{13} M_{\odot}$ that have detectable blobs more than $\sim 50\%$ of the time. Interestingly, these halo mass estimates agree with the dynamical masses, $M_{\text{dyn}} = 10^{12}-10^{13} M_{\odot}$, derived from the width of Ly α lines in similar blobs (Matsuda et al. 2006). However, special caution is required in using the Ly α line width as a mass proxy, because the radiative transfer effects on the line width are poorly understood.

For the entire blob sample (with counts of 14, 5, 3, 1 for the four survey fields), the required halo mass for $f_D = 100\%$ is $M_{\text{min}} = 0.8 \times 10^{13} M_{\odot}$. The fractional variance is $\sigma_v = 0.76$, again consistent with the observed value. Because the halo mass function is steep at the high end, M_{min} for the entire sample is similar to that derived for the bright/large blobs alone. Therefore, the resulting halo mass is insensitive to the blob selection cuts, and the statistics for our entire sample are consistent with blobs occupying halos of $\sim 10^{13} M_{\odot}$.

Halos of $\sim 10^{13} M_{\odot}$ lie in the high mass tail of the halo mass distribution at $z = 2.3$. How massive will these halos be today? Because our simulations were not run beyond $z = 1$, we consider the N-body simulation of Macciò et al. (2008), which extends to $z = 0$. Their $M_{\text{halo}} \gtrsim 10^{13} M_{\odot}$ halos grow in mass by 2–10 \times (with an average factor of 5.2 ± 2.4 increase) from $z = 2.3$ to now. Therefore, it is likely that blobs are sites for the formation of the brightest galaxies in what will become the typical halos of rich clusters ($M_{\text{halo}} \sim 10^{14} M_{\odot}$) at the present epoch.

4.4. Large-Scale Environment of Blobs

The clustering of Ly α blobs in the CDFS and the inferred large mass of their individual halos imply that blobs inhabit overdense regions. Here we test this hypothesis using the much larger population of compact Ly α emitters (LAEs) in the CDFS to trace large-scale structure over tens of comoving Mpc and thus characterize the blob environment independently. Matsuda et al. (2005) show that their blobs lie near the intersection of large-scale filamentary structures in the SSA22 overdensity. Prescott et al. (2008) use the surface number density of LAEs to show that a giant blob, originally identified via its strong MIR emission (Dey et al. 2005), resides in a region $\sim 3\times$ more dense than the edge of their survey field. We apply counts-in-cell methodology to the LAE spatial distribution in the CDFS to quantify the scale over which any structure is coherent. We then identify over-densities of LAEs relative to their average number density in the field and compare them to the spatial distribution of blobs¹³.

We select a sample of LAEs in the CDFS ($N \sim 200$ with $NB < 25.0$, excluding the blobs) following the first step in our blob selection procedure (§3), but using a $2''$ -diameter aperture to maximize the S/N of fainter point sources. In Table 1, we list the 5σ limiting magnitudes, which are determined by measuring fluxes within the randomly placed apertures in the sky background region.

Using this LAE catalog, we test whether there is structure over various spatial scales. For each scale, we count the number of LAEs within circular cells of that scale radius randomly placed over the field. Then we compare this counts-in-cells distribution with a Poisson distribution using Kolmogorov-Smirnov (K-S) statistics to check if this distribution deviates from Poisson noise. We repeat this test with different cell sizes ranging from $1'$ to $8'$. The counts-in-cells (c-in-c) distributions deviate significantly (at $> 95.0\%$ confidence) from Poisson noise for cells larger than $5'$, indicating coherent large-scale structure over scales of at least ~ 8 comoving Mpc.

Figure 12 shows the LAE distribution in the CDFS field. To estimate the overdensity of LAEs, we overlay the surface overdensity $\delta_{\Sigma} = (\Sigma - \bar{\Sigma})/\bar{\Sigma}$ contours on the map. Here $\bar{\Sigma}$ represents the average surface density estimated from all the LAE candidates over the entire field. The overdensity maps are smoothed using the adaptive kernel smoothing method developed by Ebeling et al. (2006). The FWHMs of the Gaussian filters adopted by

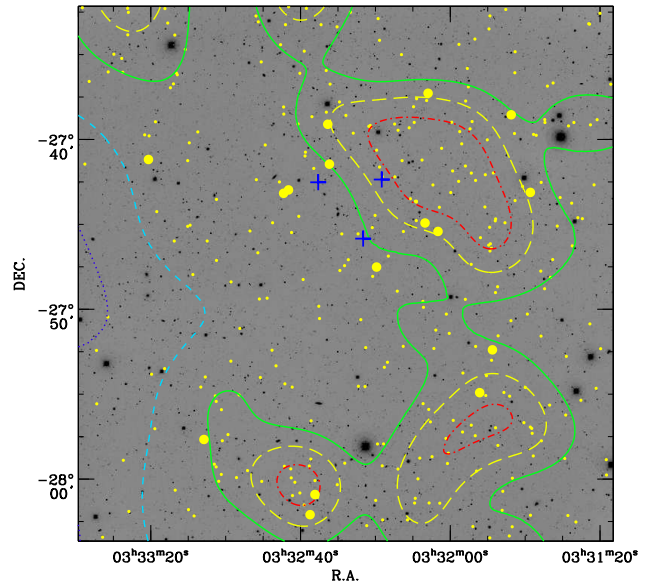


FIG. 12.— Surface density map ($\sim 30' \times 30' = 50 \text{ Mpc} \times 50 \text{ Mpc}$) of compact Ly α emitters in the CDFS. The small and big dots represent compact and extended Ly α emitters (i.e., LAEs and LABs), respectively. The contours are spaced for $\delta_{\Sigma} = (\Sigma - \bar{\Sigma})/\bar{\Sigma} = -0.7, -0.5, 0.0, 0.5, 1.0$, where $\bar{\Sigma}$ is the the average LAE surface density of the whole region. The Ly α blobs are located in the overdense region traced by the LAEs. The three crosses represent overdensities identified by Salimbeni et al. (2009) using photometric redshifts ($z_{\text{phot}} = 2.23, 2.28, 2.28$). A counts-in-cells analysis of the LAEs confirms coherent large-scale structure over scales of at least ~ 8 comoving Mpc.

this algorithm ranges from $2.8'$ to $5.2'$ depending on the local surface density of LAEs within in the field. We identify a belt-like large-scale structure elongated from north to south. The blob candidates are preferentially located within or at the boundary of this structure. Therefore, we conclude that the Ly α blobs in the CDFS indeed trace overdensities in the early universe.

Recently, Salimbeni et al. (2009) systematically searched for galaxy overdensities within the GOODS-South field up to $z \sim 2$ using photometric redshifts that have a rms accuracy of $\Delta z/(1+z) = 0.03$. In Figure 12, we show their three overdensities (crosses) with redshifts similar to our survey ($z_{\text{phot}} \simeq 2.23\text{--}2.28$). While the GOODS-South field does not include the densest part of our surface density map, their overdensities each include 19–23 members and are located near the boundary of the LAE overdensity. Spectroscopic confirmation of this system is required to relate these systems with the structures revealed by our Ly α blobs and emitters.

Further studies are required to establish that the CDFS overdensity and similar overdensities observed by other authors (e.g., Prescott et al. 2008) are in fact “proto-clusters.” For now, we note that structure in the CDFS at $z = 2.3$ is coherent over at least 8 comoving Mpc and is likely to contain tens of $\sim 10^{13} M_{\odot}$ blob halos, or at least $\sim 10^{14} M_{\odot}$ worth of mass. Were this overdensity to grow typically and virialize by $z = 0$, then its halo mass today would be like that of the rich Coma cluster, i.e., $\sim 10^{15} M_{\odot}$.

¹³ We do not detect any significant large-scale structure in the other three survey fields. Because survey depth and seeing vary over the fields, it is not clear whether the non-detections arise from a real absence of structure or poorer sensitivity.

5. CONCLUSIONS AND SUMMARY

To understand what Ly α blobs will become in the present-day universe requires that we first constrain their number density, clustering, and large-scale environment. In order to obtain unbiased measures of these quantities, we target four $\sim 30' \times 30'$ fields, Chandra Deep Field South (CDFS; Brandt et al. 2001), Chandra Deep Field North (CDFN; Giacomoni et al. 2002), and two COSMOS (Scoville et al. 2007; Koekemoer et al. 2007) subfields, with the NOAO Mayall and Blanco-4m telescopes and a custom narrowband filter designed for Ly α at $z \simeq 2.3$. The total area covered by our survey is 1.2 deg^2 . Our sensitivity and selection criteria are comparable to that of the largest previous blob survey (Matsuda et al. 2004).

We discover 25 Ly α blobs with Ly α luminosities of $L_{\text{Ly}\alpha} = 0.7\text{--}8 \times 10^{43} \text{ ergs s}^{-1}$ and isophotal areas of $A_{\text{iso}} = 10\text{--}60 \square''$. The transition from compact Ly α emitters (LAEs; $A_{\text{iso}} \sim \text{a few } \square''$) to the extended Ly α blobs ($A_{\text{iso}} > 10 \square''$) is continuous, suggesting that these two types of sources are not distinct and that whatever mechanism or mechanisms power Ly α blobs work over a wide range of luminosity and spatial extent.

Surprisingly, we find the majority of blobs (16/25) in one survey field, the CDFS. The six brightest ($L_{\text{Ly}\alpha} \gtrsim 1.5 \times 10^{43} \text{ ergs s}^{-1}$) and largest ($A_{\text{iso}} > 16 \square''$) blobs are discovered *only* in CDFS, indicating a strong field-to-field variation. Using a simple analytic approximation for the underlying fluctuations of the blob number density, we find that these large/bright blobs have a field-to-field variance of $\sigma_v \gtrsim 1.5$ (150%) about their number density of $n \sim 1.0_{-0.6}^{+1.8} \times 10^{-5} \text{ Mpc}^{-3}$. This variance is large, significantly higher than that of unresolved Ly α emitters ($\sigma_v \sim 0.3$ or 30%).

To constrain the mass of the dark matter halo around each Ly α blob, we compare the number density and clustering of blobs with the counts-in-cells distribution of halos predicted from a $1 h^{-1} \text{ Gpc}$ cosmological N-body simulation. At $z = 2.3$, n implies that bright, large blobs could occupy halos of $M_{\text{halo}} \gtrsim 10^{13} M_{\odot}$ if most halos contain a detectable blob, i.e., the detectability fraction

is $\gtrsim 50\%$. The predicted variance in n is consistent with that observed and corresponds to a bias of 7. Lower detectability fractions (e.g., $\sim 10\%$) require somewhat lower halo masses ($\sim 5 \times 10^{12} M_{\odot}$) to reproduce n , but the resulting variance is lower and further from the observed value. Blob halos lie at the high end of the halo mass distribution at $z = 2.3$ and are likely to evolve into the $\sim 10^{14} M_{\odot}$ halos typical of galaxy clusters today.

The clustering and inferred halo mass of blobs suggest that they lie in overdense environments. The spatial distribution of LAEs confirms this hypothesis: a counts-in-cells analysis of the CDFS reveals coherent large-scale structure over scales of at least ~ 8 comoving Mpc where both the LAEs and blobs cluster.

Given the strong field-to-field variance of Ly α blobs, one must be cautious in comparing blob number densities and luminosity functions among different surveys. We construct a reliable luminosity function of Ly α blobs from a deep, blind narrowband survey. Larger volume blob surveys, combined with large volume and/or higher resolution N-body simulations, will improve the constraints on blob halo mass and detectability fraction, thus discriminating among the possible energy sources of the extended Ly α emission.

We thank an anonymous referee for helpful comments. YY thanks the KPNO/CTIO staffs for observing support and the NOAO graduate student travel fund. We thank Yuichi Matsuda for providing the narrowband images of his Ly α blobs, Andrea Macciò for the halo growth function data, and Masami Ouchi for his luminosity function of LAEs. We gratefully acknowledge the assistance of Toshihiko Kimura at Asahi Spectra for his help in manufacturing our narrowband filter. AIZ acknowledges support from the NSF Astronomy and Astrophysics Research Program through grant AST-0908280 and from the NASA Astrophysics Data Analysis Program through grant NNX10AD47G.

Facilities: Mayall (MOSAIC I), Blanco (MOSAIC II)

REFERENCES

- Arnouts, S., et al. 2001, A&A, 379, 740
 Berlind, A. A., & Weinberg, D. H. 2002, ApJ, 575, 587
 Bernardeau, F., & Kofman, L. 1995, ApJ, 443, 479
 Bertin, E., & Arnouts, S. 1996, A&AS, 117, 393
 Brandt, W. N., et al. 2001, AJ, 122, 2810
 Capak, P., et al. 2004, AJ, 127, 180
 Capak, P., et al. 2007, ApJS, 172, 99
 Colbert, J. W., Teplitz, H., Francis, P., Palunas, P., Williger, G. M., & Woodgate, B. 2006, ApJ, 637, L89
 Coles, P., & Jones, B. 1991, MNRAS, 248, 1
 Dey, A., et al. 2005, ApJ, 629, 654
 Dijkstra, M., & Loeb, A. 2009, arXiv:0902.2999
 Ebeling, H., White, D. A., & Rangarajan, F. V. N. 2006, MNRAS, 368, 65
 Erben, T., et al. 2005, Astronomische Nachrichten, 326, 432
 Fardal, M. A., Katz, N., Gardner, J. P., Hernquist, L., Weinberg, D. H., & Davé, R. 2001, ApJ, 562, 605
 Francis, P. J., et al. 2001, ApJ, 554, 1001
 Gawiser, E., et al. 2006, ApJS, 162, 1
 Gawiser, E., et al. 2006, ApJ, 642, L13
 Geach, J. E., et al. 2005, MNRAS, 363, 1398
 Geach, J. E., et al. 2009, ApJ, 700, 1
 Giacomoni, R., et al. 2002, ApJS, 139, 369
 Giavalisco, M., et al. 2004, ApJ, 600, L93
 Goerdt, T., Dekel, A., Sternberg, A., Ceverino, D., Teyssier, R., & Primack, J. R. 2009, arXiv:0911.5566
 Gronwall, C., et al. 2007, ApJ, 667, 79
 Haiman, Z., & Rees, M. J. 2001, ApJ, 556, 87
 Haiman, Z., Spaans, M., & Quataert, E. 2000, ApJ, 537, L5
 Hayashino, T., et al. 2004, AJ, 128, 2073
 Hennawi, J. F., Prochaska, J. X., Kollmeier, J., & Zheng, Z. 2009, ApJ, 693, L49
 Hildebrandt, H., et al. 2006, A&A, 452, 1121
 Hogg, D. W., Cohen, J. G., Blandford, R., & Pahre, M. A. 1998, ApJ, 504, 622
 Jannuzi, B. T., & Dey, A. 1999, Photometric Redshifts and the Detection of High Redshift Galaxies, 191, 111
 Keel, W. C., Cohen, S. H., Windhorst, R. A., & Waddington, I. 1999, AJ, 118, 2547
 Keel, W. C., White, R. E., Chapman, S., & Windhorst, R. A. 2009, AJ, 138, 986
 Koekemoer, A. M., et al. 2007, ApJS, 172, 196
 Macciò, A. V., Dutton, A. A., & van den Bosch, F. C. 2008, MNRAS, 391, 1940
 Matsuda, Y., et al. 2004, AJ, 128, 569
 Matsuda, Y., et al. 2005, ApJ, 634, L125
 Matsuda, Y., Yamada, T., Hayashino, T., Yamauchi, R., & Nakamura, Y. 2006, ApJ, 640, L123
 Matsuda, Y., Iono, D., Ohta, K., Yamada, T., Kawabe, R., Hayashino, T., Peck, A. B., & Petitpas, G. R. 2007, ApJ, 667, 667
 Matsuda, Y., et al. 2009, MNRAS, 400, L66
 Monet, D. G., et al. 2003, AJ, 125, 984
 Nilsson, K. K., Fynbo, J. P. U., Møller, P., Sommer-Larsen, J., & Ledoux, C. 2006, A&A, 452, L23

- Nilsson, K. K., Tapken, C., Møller, P., Freudling, W., Fynbo, J. P. U., Meisenheimer, K., Laursen, P., Östlin, G. 2009, *A&A*, 498, 13
- Oke, J. B. 1974, *ApJS*, 27, 21
- Ouchi, M., et al. 2008, *ApJS*, 176, 301
- Ouchi, M., et al. 2009, *ApJ*, 696, 1164
- Palunas, P., Teplitz, H. I., Francis, P. J., Williger, G. M., & Woodgate, B. E. 2004, *ApJ*, 602, 545
- Peebles, P. J. E. 1980, *The Large-Scale Structure of the Universe*, (Princeton: Princeton University Press)
- Prescott, M. K. M., Kashikawa, N., Dey, A., & Matsuda, Y. 2008, *ApJ*, 678, L77
- Prescott, M. K. M., Dey, A., & Jannuzi, B. T. 2009, *ApJ*, 702, 554
- Reuland, M., et al. 2003, *ApJ*, 592, 755
- Rix, H.-W., et al. 2004, *ApJS*, 152, 163
- Saito, T., Shimasaku, K., Okamura, S., Ouchi, M., Akiyama, M., & Yoshida, M. 2006, *ApJ*, 648, 54
- Salimbeni, S., et al. 2009, *A&A*, 501, 865
- Scoville, N., et al. 2007, *ApJS*, 172, 1
- Shapley, A. E., Steidel, C. C., Pettini, M., & Adelberger, K. L. 2003, *ApJ*, 588, 65
- Shioya, Y., et al. 2009, *ApJ*, 696, 546
- Smith, D. J. B., & Jarvis, M. J. 2007, *MNRAS*, 378, L49
- Steidel, C. C., Adelberger, K. L., Shapley, A. E., Pettini, M., Dickinson, M., & Giavalisco, M. 2000, *ApJ*, 532, 170
- Taniguchi, Y. & Shioya, Y. 2000, *ApJ*, 532, L13
- Valdes, F. G. 1998, *Astronomical Data Analysis Software and Systems VII*, 145, 53
- Verhamme, A., Schaerer, D., & Maselli, A. 2006, *A&A*, 460, 397
- Weidinger, M., Møller, P., Fynbo, J. P. U., & Thomsen, B. 2005, *A&A*, 436, 825
- White, R. L., Becker, R. H., Helfand, D. J., & Gregg, M. D. 1997, *ApJ*, 475, 479
- Wolf, C., et al. 2004, *A&A*, 421, 913
- Yang, Y., Zabludoff, A. I., Davé, R., Eisenstein, D. J., Pinto, P. A., Katz, N., Weinberg, D. H., & Barton, E. J. 2006, *ApJ*, 640, 539
- Yang, Y., Zabludoff, A., Tremonti, C., Eisenstein, D., & Davé, R. 2009, *ApJ*, 693, 1579

TABLE 1
NARROWBAND OBSERVATIONS

| Field | R.A. (J2000) | Dec. (J2000) | Observing Date | Telescope | Exposure (hour) | Depth ^a (AB mag) | Survey Area | Seeing | Pixel Scale ^b |
|---------|-----------------|-----------------|----------------|-----------|--------------------|--------------------------------|-------------|--------|--------------------------|
| CDF-S | 03:32:27.8 | -27:47:56 | Nov. 2007 | Blanco 4m | 10 | 25.65 | 31'6 × 31'6 | 1.0'' | 0''27 |
| CDF-N | 12:36:50.9 | 62:11:48 | May 2007 | Mayall 4m | 10 | 25.27 | 29'5 × 29'5 | 1.3'' | 0''30 |
| COSMOS1 | 09:59:16.9 | 01:55:19 | Feb. 2009 | Blanco 4m | 7.7 | 25.27 | 36'0 × 36'3 | 1.2'' | 0''27 |
| COSMOS2 | 09:59:16.8 | 02:31:19 | Feb. 2009 | Blanco 4m | 7.2 | 25.25 | 36'0 × 36'3 | 1.2'' | 0''27 |

^a 5σ detection limit for 2''-diameter aperture.

^b Pixel scales of final combined images, which are determined by the largest pixel scale between narrowband and broadband images.

TABLE 2
SUMMARY OF BROADBAND IMAGES

| Field | Band | Effective Wavelength (Å) | Band Width (Å) | Depth (AB mag) | Seeing (arcsec) | Telescope and Instrument | Reference |
|--------|----------|-----------------------------|-------------------|-------------------|--------------------|--------------------------|------------------------|
| CDF-S | <i>U</i> | 3505 | 626 | 26.0 ^a | 1.05 | ESO 2.2m WFI | Gawiser et al. (2006b) |
| | <i>B</i> | 4600 | 915 | 26.9 | 0.95 | ESO 2.2m WFI | |
| CDF-N | <i>U</i> | 3648 | 387 | 27.1 ^b | 1.26 | KPNO MOSAIC I | Capak et al. (2004) |
| | <i>B</i> | 4428 | 622 | 26.9 | 0.71 | Subaru Suprime-Cam | |
| COSMOS | <i>U</i> | 3798 | 720 | 26.4 ^b | 0.90 | CFHT Megaprime | Capak et al. (2007) |
| | <i>B</i> | 4460 | 897 | 27.3 | 0.95 | Subaru Suprime-Cam | |

^a CDF-S: 5σ detection limit corrected for infinite aperture.

^b CDF-N and COSMOS 5σ detection limit for 3'' diameter aperture.

TABLE 3
PROPERTIES OF Ly α BLOB CANDIDATES

| ID | R.A. (J2000) | Dec. (J2000) | L_{tot} (10^{43} ergs s ⁻¹) | L_{iso} (10^{43} ergs s ⁻¹) | Area (\square'') | Note |
|---------------------------------------|-----------------|-----------------|--|--|-------------------------|-----------|
| Extended Chandra Deep Field South | | | | | | |
| CDFS-LAB01 | 03 32 36.1 | -28 00 54.5 | 7.81 ± 0.28 | 8.00 | 61.6 ± 3.7 | confirmed |
| CDFS-LAB02 | 03 33 20.6 | -27 41 10.8 | 3.26 ± 0.17 | 2.88 | 37.9 ± 3.3 | confirmed |
| CDFS-LAB03 | 03 31 52.1 | -27 54 54.6 | 3.23 ± 0.29 | 2.72 | 43.2 ± 4.4 | |
| CDFS-LAB04 | 03 32 05.9 | -27 37 16.7 | 2.64 ± 0.15 | 2.40 | 30.9 ± 2.1 | confirmed |
| CDFS-LAB05 | 03 31 48.7 | -27 52 23.3 | 1.72 ± 0.39 | 1.14 | 21.3 ± 6.2 | |
| CDFS-LAB06 | 03 32 19.6 | -27 47 30.8 | 1.53 ± 0.11 | 1.57 | 16.5 ± 1.8 | |
| CDFS-LAB07 | 03 32 03.2 | -27 45 25.0 | 1.48 ± 0.17 | 1.56 | 18.5 ± 2.5 | |
| CDFS-LAB08 | 03 31 43.7 | -27 38 32.9 | 1.21 ± 0.22 | 1.32 | 19.3 ± 4.5 | |
| CDFS-LAB09 | 03 32 44.5 | -27 43 10.2 | 1.17 ± 0.15 | 0.87 | 14.3 ± 2.0 | |
| CDFS-LAB10 | 03 32 37.4 | -28 02 05.7 | 1.14 ± 0.25 | 0.71 | 12.6 ± 2.6 | confirmed |
| CDFS-LAB11 | 03 32 43.2 | -27 42 58.3 | 1.09 ± 0.08 | 1.02 | 10.3 ± 1.3 | |
| CDFS-LAB12 | 03 32 06.7 | -27 44 55.2 | 1.08 ± 0.16 | 0.73 | 13.3 ± 2.4 | |
| CDFS-LAB13 | 03 32 32.7 | -27 39 06.3 | 1.03 ± 0.09 | 0.94 | 12.0 ± 1.5 | |
| CDFS-LAB14 | 03 32 32.2 | -27 41 27.2 | 0.98 ± 0.09 | 0.93 | 12.8 ± 1.5 | confirmed |
| CDFS-LAB15 | 03 31 38.6 | -27 43 07.0 | 0.96 ± 0.08 | 0.81 | 11.8 ± 1.1 | |
| CDFS-LAB16 | 03 33 05.8 | -27 57 40.0 | 0.69 ± 0.18 | 0.62 | 10.3 ± 3.0 | |
| Chanda Deep Field North | | | | | | |
| CDFN-LAB01 | 12 35 35.2 | +62 14 28.5 | 1.31 ± 0.11 | 1.30 | 13.2 ± 1.8 | |
| CDFN-LAB02 | 12 35 30.2 | +62 01 39.2 | 1.15 ± 0.12 | 0.94 | 11.7 ± 1.7 | marginal? |
| CDFN-LAB03 | 12 36 09.9 | +61 57 16.6 | 1.01 ± 0.12 | 0.94 | 12.2 ± 1.9 | marginal? |
| CDFN-LAB04 | 12 36 59.2 | +62 24 35.2 | 0.99 ± 0.15 | 0.80 | 13.0 ± 2.0 | |
| CDFN-LAB05 | 12 38 18.4 | +62 04 04.1 | 0.72 ± 0.13 | 0.61 | 11.1 ± 1.9 | |
| Cosmic Origins Evolution Survey Field | | | | | | |
| COSMOS-LAB01 | 09 59 23.9 | +01 55 11.7 | 1.24 ± 0.19 | 0.87 | 14.6 ± 5.2 | marginal? |
| COSMOS-LAB02 | 09 59 14.2 | +01 48 43.1 | 0.92 ± 0.19 | 1.05 | 11.9 ± 2.3 | marginal? |
| COSMOS-LAB03 | 09 58 12.8 | +01 52 56.2 | 0.84 ± 0.16 | 0.70 | 12.5 ± 2.5 | |
| COSMOS-LAB04 | 09 58 49.6 | +02 30 49.9 | 1.01 ± 0.13 | 0.92 | 11.8 ± 2.1 | |

NOTE. — The note column indicates whether the redshifts of the candidates are spectroscopically confirmed with the Ly α and/or H α line and whether they are marginally resolved (labelled “marginal”).

TABLE 4
 BLOB STATISTICS

| | CDFS | CDFN | COSMOS1 | COSMOS2 |
|--|-------|-------|---------|---------|
| $A_{\text{iso}} > 16 \square''$ | 8 | 0 | 0 | 0 |
| $A_{\text{iso}} = 10\text{--}16 \square''$ | 8 | 5 | 3 | 1 |
| N_{blob} (bright/large sample) ^a | 6 | 0 | 0 | 0 |
| N_{blob} (entire sample) | 14 | 5 | 3 | 1 |
| Effective area [deg ²] | 0.270 | 0.241 | 0.352 | 0.362 |

^a N_{blob} is the number of blobs corrected to the same depth and seeing for all four survey fields. We use N_{blob} for estimating the number density, its variance, and the blob halo mass in §4.3.1.

 TABLE 5
 FIELD-TO-FIELD VARIANCE AND NUMBER DENSITY OF BLOBS

| | Variance σ_v | | | Number per 0.25 deg ² \bar{N} | | |
|--|---------------------|------|------|--|------|-------------|
| | Min | Best | Max | Min | Best | Max |
| Bright, Large Blobs with $A_{\text{iso}} > 16 \square''$ | | | | | | |
| Joint | 1.49 (0.58) | ... | ... | 0.27 | ... | ... |
| Marginal | 3.11 (0.99) | ... | ... | 0.40 (0.17) | 1.15 | 3.27 (8.30) |
| Entire Sample with $A_{\text{iso}} > 10 \square''$ | | | | | | |
| Joint | 0.26 (0.10) | 0.87 | 5.21 | 2.27 (1.56) | 4.76 | 21.7 |
| Marginal | 0.57 (0.31) | 1.20 | 3.51 | 2.91 (2.13) | 4.76 | 10.3 (27.1) |

NOTE. — The number density \bar{N} represents the number of blobs per 0.25 deg². In the parentheses, we list the 2σ limits.

 TABLE 6
 CUMULATIVE LUMINOSITY FUNCTION OF LY α BLOBS

| $\text{Log}(L_{\text{Ly}\alpha})$ | $n(> L) [\times 10^{-5} \text{Mpc}^{-3}]$ | | |
|-----------------------------------|---|------------------|--------------------|
| | CDFS ^a | All ^b | SSA22 ^c |
| 43.90 | ... | ... | 1.54 ± 1.09 |
| 43.70 | 0.83 ± 0.83 | 0.18 ± 0.18 | 2.31 ± 1.33 |
| 43.50 | 2.50 ± 1.44 | 0.55 ± 0.32 | 3.08 ± 1.54 |
| 43.30 | 3.33 ± 1.67 | 0.73 ± 0.37 | 5.38 ± 2.04 |
| 43.10 | 5.83 ± 2.20 | 1.47 ± 0.52 | 10.77 ± 2.88 |
| 42.90 | 12.49 ± 3.22 | 4.23 ± 0.88 | 18.46 ± 3.77 |
| 42.70 | 13.32 ± 3.33 | 4.59 ± 0.92 | 26.92 ± 4.55 |

^a LF from blobs in CDFS.

^b LF from all four survey fields (CDFS, CDFN, COSMOS1, and COSMOS2).

^c We also list the LF from Matsuda et al. (2004) for comparison.

TABLE 7
COUNTS-IN-CELLS DISTRIBUTION FOR BRIGHT, LARGE BLOBS

| f_D (1) | $M_{\min}(M_{\odot})$ (2) | σ_v (3) | N-Body Simulation | | | Poisson Distribution | | |
|--------------|------------------------------|-------------------|-------------------|----------------------|--------------------|----------------------|----------------------|--------------------|
| | | | $P(N=0)$ (4) | $P(N \geq 6)$ (5) | Probability (6) | $P(N=0)$ (7) | $P(N \geq 6)$ (8) | Probability (9) |
| 100% | 1.66×10^{13} | 1.03 | 41.5% | 4.40% | 1.25% | 23.3% | 0.440% | 0.022% |
| 50% | 1.16×10^{13} | 0.93 | 38.5% | 3.65% | 0.83% | 22.9% | 0.370% | 0.018% |
| 25% | 7.97×10^{12} | 0.83 | 35.8% | 3.27% | 0.60% | 23.4% | 0.300% | 0.015% |
| 12.5% | 5.32×10^{12} | 0.76 | 35.6% | 2.51% | 0.45% | 23.8% | 0.370% | 0.020% |

NOTE. — (1) detectability fraction, (2) dark matter halo mass, (3) variance [Eq. (2)], (4) probability of non-detection, (5) probability of finding 6 or more blobs, (6) posterior probability of finding 6 or more blobs in one field and none in the three other fields, (7)–(9) same as (4)–(6) but for Poisson distribution.

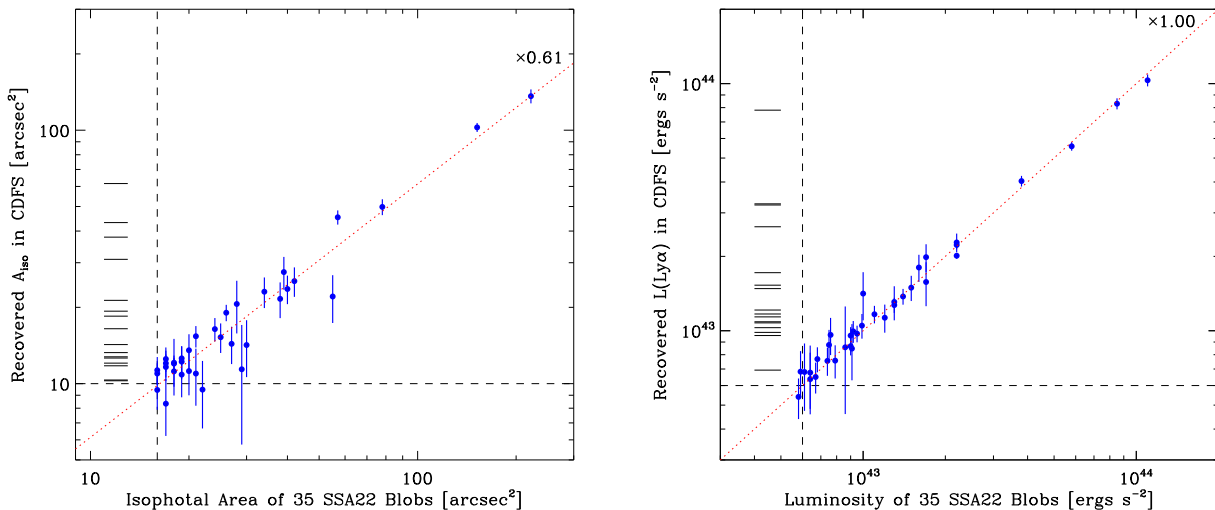


FIG. 13.— Comparison in $L_{\text{Ly}\alpha}$ and A_{iso} between our 16 CDFS blobs (horizontal bars) and the 35 Matsuda et al. (2004) blobs in the SSA22 field (filled circles). The vertical and horizontal dashed lines indicate the size selection criteria for the extended sources adopted by Matsuda et al. (2004) and by our work, respectively. The dotted lines represent the average ratios (~ 0.61 and 1.0) between originally reported and the recovered values in A_{iso} and $L_{\text{Ly}\alpha}$. The recovery test of the Matsuda et al. (2004) blobs when pasted into our CDFS field shows that we can detect all blobs like theirs in our survey.

APPENDIX

COMPARISON WITH MATSUDA ET AL. $\text{Ly}\alpha$ BLOB SAMPLE

It is difficult to compare the properties of $\text{Ly}\alpha$ blob samples among different surveys because of non-uniform selection criteria and different imaging depth. Here we compare our $z = 2.3$ sample to that of Matsuda et al. (2004) at $z = 3.1$. We repeat the procedures for the recovery test described in §3 (see also Yang et al. 2009), pasting thumbnail images provided by Matsuda et al. (2004) into our CDFS image. Because the narrowband filter bandwidths of the two surveys are similar, we do not make any correction for the difference in filter transmission, but we scale the apparent size and the surface brightness accounting for the different redshifts.

Figure 13 shows the $\text{Ly}\alpha$ luminosity and isophotal area recovered from this test as a function of the input $L_{\text{Ly}\alpha}$ and A_{iso} for the 35 Matsuda et al. (2004) blobs. Due to the slightly shallower depth of our survey, the Matsuda et al. blobs would look smaller by a factor of 61% than the originally reported sizes. Note that one expects a 86% decrease in area purely from the differences in angular diameter distance between two survey redshifts. The vertical and horizontal dashed lines indicate the size selection criteria for the extended sources adopted by Matsuda et al. (2004) and by our work, respectively. Most Matsuda et al. (2004) blobs are recovered as larger than $10''$, confirming the capability of our survey for detecting them. The line luminosities are also recovered well, so there is no bias in the luminosity measurements.